Lawrence Berkeley Laboratory
UNIVERSITY OF CALIFORNIA

ENERGY & ENVIRONMENT DIVISION

LASER SPECTROSCOPY AND TRACE ELEMENT ANALYSIS

Chapter from the Energy and Environment Division Annual Report 1980

May 1981

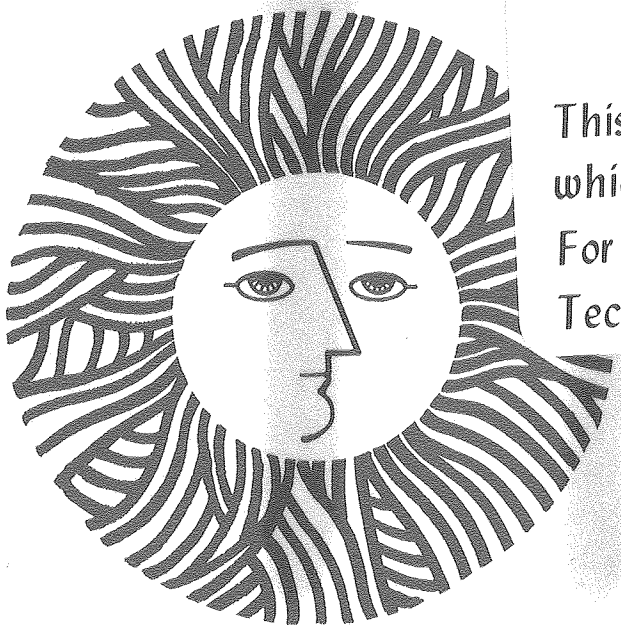

Prepared for the U.S. Department of Energy under Contract W-7405-ENG-48

DISCLAIMER

LASER SPECTROSCOPY AND TRACE ELEMENT ANALYSIS
FY 1980

Lawrence Berkeley Laboratory
University of California
Berkeley, California 94720

Prepared for the U.S. Department of Energy under Contract W-7405-ENG-48.

CONTENTS

LASER SPECTROSCOPY AND TRACE ELEMENT ANALYSIS PERSONNEL

L. Alvarez
N. Amer
F. Asaro
N. Bergstrom
C. Case
R. Clem
R. Gerlach
R. Giauque
W. Jackson
R. Johnson
S. Kohn
R. McLaughlin
H. Michel
A. Nero
M. Olmstead
F. Park
S. Phillips
M. Quinby-Hunt
D. Wake
Z. Yasa

INTRODUCTION

Energy production and utilization result in the emission of pollutants that are potentially harmful to man and to other forms of life. It is desirable to provide means to measure these pollutants, to understand their fate, and to assess their effects on health and other biological activities such as agriculture.

In order to control these pollutants, adequate methods are required for monitoring the level of various substances often present at low concentrations. The Energy and Environment Division Applied Research in Laser Spectroscopy & Analytical Techniques Program is directed toward meeting these needs. Emphasis is on the development of physical methods, as opposed to conventional chemical analysis techniques. The advantages, now widely recognized, include ultra-high sensitivity coupled with minimal sample preparation. In some instances physical methods provide multi-parameter measurements which often provide the only means of achieving the sensitivity necessary for the detection of trace contaminants.

APPLIED PHYSICS AND LASER SPECTROSCOPY RESEARCH

N. Amer, N. Bergstrom, R. Gerlach, W. Jackson, R. Johnson, S. Kohn, M. Olmstead, C. Rosenblatt,† D. Wake, and Z. Yasa*

OVERVIEW

The research philosophy of our group is to apply the knowledge of advanced laser spectroscopy and condensed matter physics to energy and environmental problems. Because of the narrow linewidth and tunability of lasers, unsurpassed sensitivity and specificity can be achieved in detecting trace contaminants of the environment. The advanced state of condensed matter physics makes it possible to apply such knowledge to energy production and to test novel methods for energy conversion such as photovoltaic solar cells, superionic electrical energy storage devices, and the recovery and extraction of oil from abandoned wells and oil shales with lyotropic liquid-crystal emulsifiers.

LASER PHOTOACOUSTIC AND PHOTOTHERMAL MEASUREMENTS AND CHARACTERIZATION‡

Laser photoacoustic and photothermal spectroscopies provide a powerful tool for the detection of trace contaminants in air and water, as well as a means for investigating the fundamental properties of gaseous, liquid, or solid phases of matter. One of our goals in this project is to develop ultrasensitive, multiparameter, elemental and molecular detectors for the characterization of pollutants released in the process of energy production and utilization. Another aim is to maintain a state of the art capability in photoacoustic and photothermal detections by fully understanding the physics of these techniques. Concurrent with these efforts, we are actively developing new or modified laser systems compatible with our particular needs. Below, we report our results for FY 1980.

PHOTOTHERMAL DEFLECTION SPECTROSCOPY AND DETECTION: THEORY§

Before proceeding with the theoretical treatment of photothermal deflection spectroscopy (PDS), a brief physical description of PDS is in order. The absorption of the optically exciting beam (pump beam) causes a corresponding change in the index of refraction of the optically heated region. The absorption also causes an index-of-refraction gradient in a thin layer adjacent to the sample surface. By probing the gradient of the varying index of refraction with a second beam

---

*Group Leader

†Present Address: National Magnet Laboratory, M.I.T., Cambridge, Mass.

‡This work was supported by the Assistant Secretary for Environment, Office of Health and Environmental Research, Pollutant Characterization and Safety Research Division of the U.S. Department of Energy under Contract No. W-7405-ENG-48.

§Complete version of this report is given in LBL-11541 and will be published in Applied Optics, April 15, 1981.

(probe beam), one can relate its deflection to the optical absorption of the sample. This is in contrast with probing thermally induced changes in optical path lengths, as in interferometric techniques, or probing the curvature of the index of refraction, as in thermal lensing (TL). As can be seen from the above description, one has two choices in performing PDS: (1) collinear photothermal deflection, where the gradient of the index of refraction is both created and probed within the sample (Fig. 1), or (2) transverse photothermal deflection, where the probing of the gradient of the index of refraction is accomplished in the thin layer adjacent to the sample--an approach most suited for opaque samples and for materials of poor optical quality (Fig. 1).

The calculation of the expected beam deflection for PDS can be divided into two parts. One first finds the temperature distribution in the sample and then solves for the optical beam propagation through an inhomogeneous medium. Below, we give the solutions for the probe beam deflection for various experimental configurations.

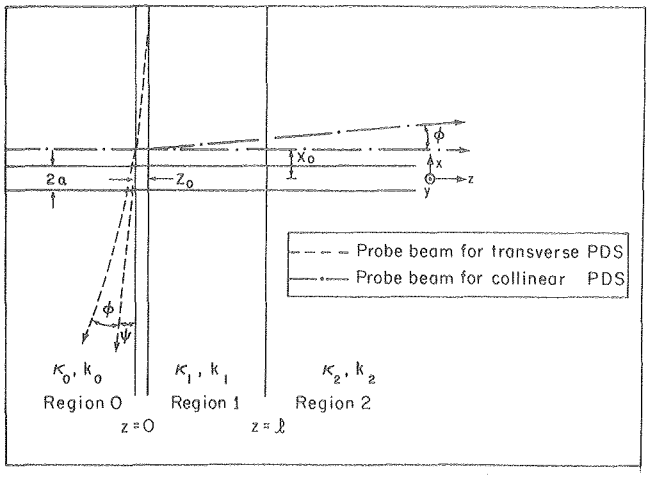

Fig. 1. Geometry for theory. The heat deposited diffuses into Region 0 and Region 2 as well as radially. For transverse PDS, the probe beam may be displaced along the y axis by a distance y_o. (XBL 8012-2089)

Solution for Beam Deflection

Collinear PDS. For collinear PDS, the beam is deflected by the temperature gradient in all three regions. For simplicity, we assume that the probe beam travels parallel to the pump beam axis and is deflected only in Regions 1 and 2. However, the interaction length is restricted to be consistant with an angle between the pump and probe beams (see Fig. 2).

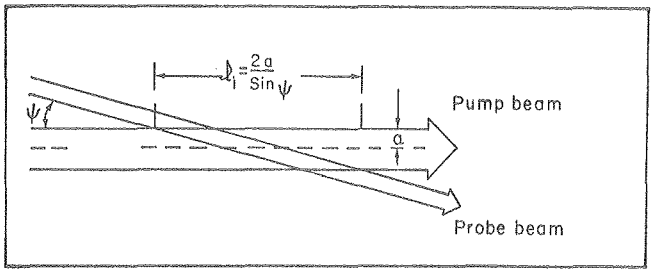

Fig. 2. Effective intersection length for collinear PDS. (XBL 8010-2083)

The deflection in this case is given by:

$$\phi = \frac{-e^{i\omega t}}{2n_o}\frac{\partial n}{\partial T}\left[\int_o^{\ell} dz \int_o^{\infty} \delta^2\, d\delta J_1(\delta x_o)\ \Gamma(\delta)\ e^{-\alpha z} + A(\delta)\ e^{-\beta_1 z} + B(\delta)\ e^{\beta_1 z} + \right.$$

$$\left. \int_o^{\ell_i} dz \int_o^{\infty} \delta^2 J_1(\delta x_o)\ d\delta D(\delta)\ e^{-\beta 2(z-\ell)}\right] + \text{c.c.}\quad \ell_i > \ell \qquad (1)$$

where $\ell_i = 2a/\sin\psi$ is the length of interaction of the two beams, x_o is the displacement between the beams, and ψ is the angle of their intersection. If the beams overlap in Region 1 only, then

$$\phi = -\frac{1}{2n_o}\frac{\partial n}{\partial T} e^{i\omega t} \int_o^{\ell_i} dz \int_o^{\infty} \delta^2\, d\delta J_1(\delta x_o)\left[\Gamma(\delta)\ e^{-\alpha z} + A(\delta)\ e^{-\beta_1 z} \quad B(\delta)\ e^{\beta_1 z}\right] + \text{c.c.}\quad \ell_i < \ell \qquad (2)$$

Transverse PDS. For transverse PDS, the probe beam propagates completely within Region 0. The probe beam path (Fig. 1) is the deflection in this case and is given by

$$\phi = \frac{1}{2}\frac{e^{i\omega t}}{n_o}\frac{\partial n}{\partial T}\int_{\infty}^{-z_o/(\tan\psi)} dz \int_{o}^{\infty} \delta J_o\left(\delta\sqrt{y_o^2 + x^2}\right)\beta_o E(\delta)\, e^{\left|(\tan\psi)x+z_o\right|\beta_o} + c.c. \qquad (3)$$

SENSITIVE IN-SITU TRACE GAS DETECTION BY PHOTOTHERMAL DEFLECTION SPECTROSCOPY†

This work presents an approach to photothermal deflection spectroscopy where the refractive index gradient is both created and optically detected within the medium of interest (in this case a gas). Such an approach proved to be sensitive and suited for the in-situ detection of trace gases since it obviates enclosing the sample in some container in order to perform the detection.

Using diffraction theory, we have recently shown that, for modulation of the pump beam at low frequency, the amplitude ϕ of the probe beam deflection is given by

$$\phi = (dn/dT)(P/\kappa\pi^2 x_o)\left[1-\exp(-\alpha\ell)\right]\left[1-\exp(-x_o^2/a^2)\right] \qquad (1)$$

where dn/dT is the temperature coefficient of refractive index, P is the amplitude of the incident laser power modulation, κ is the thermal conductivity of the gas, x_o is the distance between the intensity maxima of the pump and probe beams, α is the optical absorption coefficient, ℓ is the interaction length of the pump and probe beams, and a is the radius of the pump beam at 1/e intensity. Thus, for small $\alpha\ell(\lesssim 2)$ the amplitude of the deflection is proportional to $\alpha\ell$ and to the power. Furthermore, ϕ exhibits a maximum near $x_o/a \sim 1$ defining the optimal separation between the pump and probe beams.

To investigate the sensitivity of photothermal deflection spectroscopy for the detection of small absorption in gases, we chose to determine the minimal detectable concentration of ethylene at a signal to noise ratio (S/N) of unity. We also tested the in-situ capability of this detection scheme by measuring the absorption spectrum of laboratory air (without any sample cell or enclosure) in the 9-11 μm region of the infrared.

The experimental arrangement is shown in Figure 3. To determine the sensitivity and obtain a calibration of the apparatus, we initially employed a calibrated mixture of ethylene in nitrogen and other lower-concentration mixtures obtained by dilution of the calibration mixture in a 20 cm long cell. In Figure 4, we plot signal from the photodiode as a function of ethylene concentration. As can be seen, the detected signal is a linear function of the concentration over four orders of magnitude. No coherent background signal was detected when the cell was filled only with nitrogen.

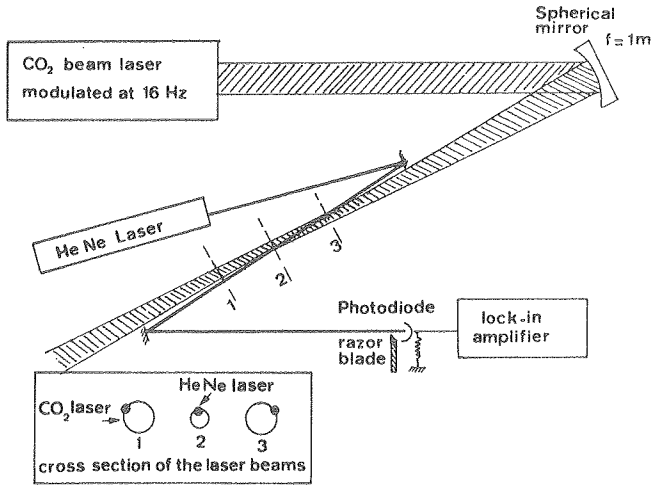

Fig. 3. Schematic of experimental equipment. (XBL 813-8370)

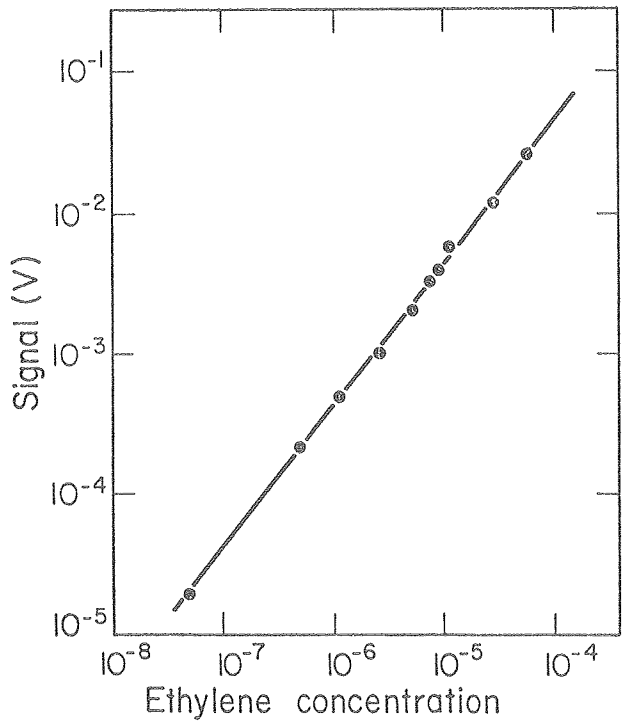

Fig. 4. Thermal deflection signal versus ethylene concentration in nitrogen (molar fraction). (XBL 813-8371)

†Complete version of this work appeared in Applied Physics Lett., vol. 37, no. 519 (1980).

From these results, we compute a minimum detectivity (S/N=1) of 5 ppb, i.e., a minimum absorption coefficient detection of $\sim 10^{-7}$ cm^{-1}.

We also measured, in situ, the absorption spectrum of laboratory air using the various lines of the R branches of the 9.4 μm and 10.4 μm bands of CO_2 lasers. Tables 1 and 2 compare our results with published data. Although the dominant contribution to the absorption in the 9.4 μm region can be interpreted as due to water vapor, other unidentified gases appear to contribute significant absorption in the 10 μm region.

Table 1. Observed signal for laboratory air in the 9.4 μm band of the $C^{12}O_2^{16}$ laser.

Laser line	Frequency (cm^{-1})	Experimental absorption coefficient[a] (10^{-6} cm^{-1})	Abs. coeff. of water vapor (10^{-6} cm^{-1})
R(10)	1071.884	2.9	0.35
R(12)	1073.278	1.5	0.44
R(14)	1074.646	2.3	1.48
R(16)	1075.988	1.45	0.57
R(18)	1077.303	1.35	0.43
R(20)	1078.591	1.2	0.40
R(22)	1079.852	1.51	0.40
R(24)	1081.087	1.65	0.39
R(26)	1082.296	1.2	0.36
R(28)	1083.479	1.3	0.38
R(30)	1084.635	2.6	1.40
R(32)	1085.765	3.0	0.58

[a]Data were normalized to published data for the R(20) line of the 10.4 μm band.

Table 2. Observed signal for laboratory air in the 10.4 μm band of the $C^{12}O_2^{16}$ laser.

Laser line	Frequency (cm^{-1})	Experimental absorption coefficient[a] (10^{-6} cm^{-1})	Abs. coeff. of water vapor (10^{-6} cm^{-1})
R(8)	967.707	0.55	0.41
R(10)	969.139	0.65	0.34
R(12)	970.547	1.5	0.97
R(14)	971.930	1	0.92
R(16)	973.289	1.1	0.78
R(18)	974.622	0.75	0.61
R(20)	975.930	5.5	5.49
R(22)	977.214	0.85	0.84
R(24)	978.472	0.65	0.50
R(26)	979.705	0.68	0.49
R(28)	980.913	0.68	0.40
R(30)	982.096	1	0.46
R(32)	982.252	0.95	0.40

[a]Data were normalized to published data for the R(20) line of the 10.4 μm band.

Our detection limits were set by the following factors:

- Fluctuations in the pointing stability of the probe beam were estimated to be two orders of magnitude above the photon noise. This limitation can be alleviated, for example, by the inclusion of an intracavity iris to force the laser to oscillate on the fundamental transverse mode.
- In the case of experiments requiring long beam paths, air turbulence can be a limiting factor when the pump beam is modulated at low frequencies. Introduction of a Fabry-Perot interferometer as close as possible to the interaction region should overcome this problem. Another simple solution is to have the two laser beams intercept each other inside an open ended tube.
- Electronic noise was a limiting factor only when a position-sensing detector was used.
- With adequate isolation, mechanical vibrations do not set the detection limit.

In conclusion, we have shown that photothermal deflection spectroscopy provides a simple means for the measurement of very weak absorptions in gas phase samples. We have also demonstrated its feasibility for in-situ measurements, i.e., in the absence of a sample container, thus eliminating the problems associated with sampling techniques. This technique also eliminates the background signal associated with scattering and with the heating of the sample cell windows which one encounters in photoacoustic spectroscopy.

SENSITIVE PHOTOTHERMAL DEFLECTION SPECTROSCOPY OF CONDENSED MEDIA[†]

When an intensity modulated beam of electromagnetic radiation (pump beam) is incident on an absorbing medium, heating will ensue. Concomitant with this time-dependent change in the medium temperature is a corresponding modulated index of refraction gradient which can be employed to deflect a probe beam intersecting the pump beam within the sample and/or substrate. The deflection can be as small as 10^{-9} - 10^{-10} radians, which is well within the detectivity levels of available position sensors. The amplitude of the deflection is related to the optical absorption in a straightforward manner.

Using diffraction theory, we have derived general expressions for the deflection of a laser beam by an absorbing medium on a given substrate. A very brief description of this theory is given on page 1. Neglecting the effects of the substrate and considering the case where the thermal diffusion length of the medium is much smaller than the Gaussian pump beam radius (the case of high frequency modulation and/or low thermal con-

[†]Complete version of this work appeared in Optics Lett. vol. 5, no. 377 (1980).

ducting medium), the deflection angle ϕ is given by

$$\phi = (dn/dT)(P/\omega\rho c\pi^2 a^2)\left[1-\exp(-\alpha\ell)\right]\left[-2x_o/a^2)\exp(-x_o^2/a^2)\right] \qquad (1)$$

where dn/dT is the temperature coefficient of the index of refraction of the medium, P is the incident laser power, ω is the angular modulation frequency of the pump beam, ρc is the heat capacity per unit volume, a is the radius of the pump beam at 1/e intensity, x_o is the separation between the intensity maxima of the pump and probe beams, α is the optical absorption coefficient, and is the optical path length in the absorbing medium. Thus, for small $\alpha\ell$ ($\lesssim 2$) the deflection amplitude is proportional to the optical absorption and to the power, while inversely proportional to the modulation frequency. Furthermore, ϕ exhibits a maximum near $x_o/a \sim 1$ defining the optical separation between the pump and probe beams.

On the other hand, in the case where the thermal diffusion length is much larger than the pump beam radius, ϕ is given by

$$\phi = (dn/dT)(P/\kappa\pi^2 x_o)\left[1-\exp(-\alpha\ell)\right]\left[1-\exp(-x_o^2/a^2)\right] \qquad (2)$$

where κ is the thermal conductivity of the medium. Note that in this case, ϕ is independent of ω. The experimental arrangement is shown in Figure 5.

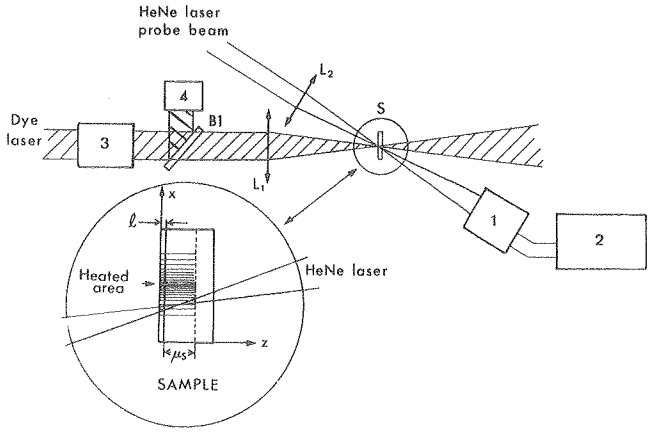

Fig. 5. Schematic of experimental equipment.
1 - Position sensor
2 - Lock-in amplifier
3 - Modulator
4 - Power meter
L_1 - 12-cm focal length lens
L_2 - 6-cm focal length lens
B_1 - Beam splitter

(XBL 806-1128)

In Figure 6, we present the amplitude of the deflection as a function of the distance from the center of the optically heated region. The results are given for low (5 Hz) and high (5 kHz) modulation frequencies. As predicted by Equations (1) and (2), the optically heated region is much larger than the waist of the pump beam at low frequency. On the other hand, at high modulation frequency, the pump beam waist and the heated region are of comparable dimensions.

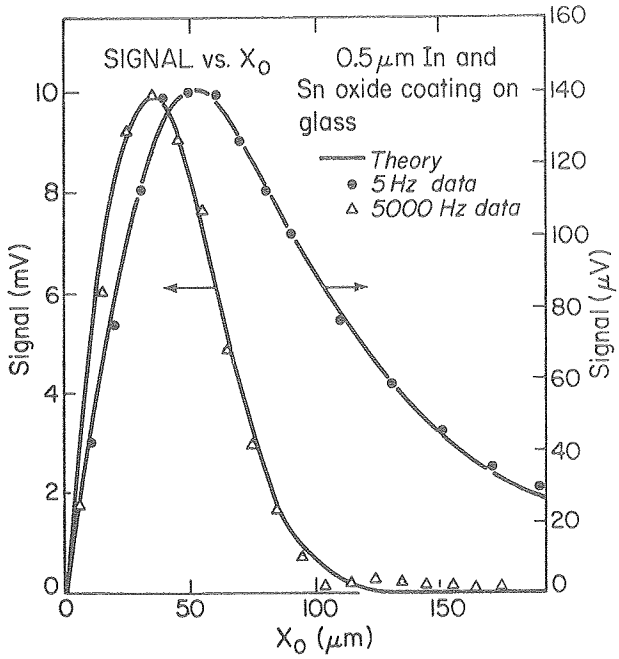

Fig. 6. Thermal deflection signal vs. the separation between the pump beam and the probe beam. The solid lines are the results of the theory.
(XBL 804-577)

To deduce the minimum detectable absorption coefficient, we compared the wavelength dependence of the photothermal deflection with the absorbance of the film when measured with a Cary 17 spectrophotometer. The film consisted of a 0.5μ thick mixture of 80% indium oxide and 20% tin oxide and was deposited on a glass substrate. At the maximum absorption, we found that for an average power of 100 mW and a time constant of 3 seconds, the noise equivalent signal was $\alpha\ell \sim 2 \times 10^{-7}$. This implies a minimum detectable absorbed power of 8×10^{-8} W/Hz$^{1/2}$. Using the value of the absorption measured by the Cary spectrophotometer, we derived a calibration relating absorption coefficients to the measured voltage output of the position sensor. Similar sensitivities were achieved with a 2μ film of CdS deposited on a glass substrate.

We have also measured the absorption spectra of bulk liquid samples. In this case, the optically heated medium is directly probed with the He - Ne laser. In Figure 7-a, we present the absorption spectrum of the 6th harmonic of the C-H stretching excitation of neat benzene, filtered through 0.22 millipore filter. Using a Cary 17 spectrophotometer, the calibration factor for the absolute absorption was determined from a long-

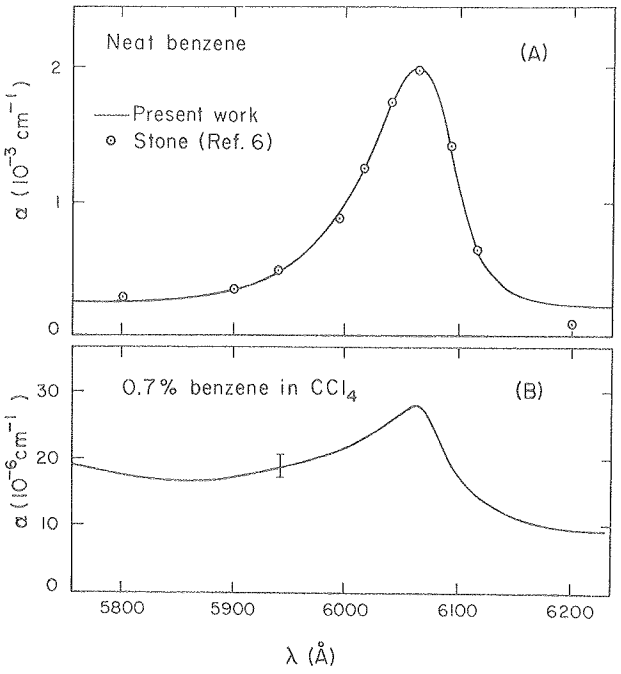

Fig. 7. a. The absorption spectrum of the 6th harmonic of the C-H stretching excitation of neat benzene. ℓ = 0.5 mm. Beam power = 60 mW.

b. The absorption of 0.7% benzene in CCl_4. ℓ = 0.5 mm. Beam power = 60 mW. Lock-in amplifier time constant = 0.3 seconds. Bar represents typical errors of $\pm$ 2×10^{-6} cm^{-1}.

(XBL 806-1127)

optical-path absorption measurement at the peak of this absorption band. As can be seen from the figure, both the line shape and strength of the absorption agree well with published results. To determine the minimum detectable absorption coefficient, we diluted the benzene (0.7%) in carbon tetrachloride (see Fig. 7-b). The noise equivalent absorption was 2×10^{-6} cm^{-1} for a pump beam of 60 mW and a 0.3 second time constant. Hence, our noise equivalent absorption is 1.5×10^{-7} cm^{-1} $W/Hz^{1/2}$. Since the optical path length ℓ was only 0.5 mm, this demonstrates that $\alpha\ell$ values of 10^{-8} are measurable by this technique. The increased detectivity in the case of liquids is due to their typically larger dn/dT values when compared with those of solids.

To check for saturation of the signal, we measured the absorption of a 0.5 mm didymium glass in the 5900 Å region. We found, as predicted by our theory, that the deflection amplitude depends linearly on α for $\alpha\ell \simeq 1-\exp(-\alpha\ell)$, beyond which signal saturation sets in.

Factors setting the limits of our sensitivity were:

- In the case of low frequency modulation, the pointing stability of the probe laser was the limiting factor. This limitation can be alleviated, for example, by the insertion of an intracavity iris to force the laser to oscillate on the fundamental transverse mode. At high frequency modulation, the limits were set by the stability of the probe laser and by the electronic noise of the position sensor.
- Care must be taken to avoid overlapping the two beams on the window of the liquid cell, otherwise a significant background signal is observed.
- With reasonable isolation, mechanical vibration was not a limiting factor.

In conclusion, we have described in this summary a simple photothermally based method for the determination of very small absorption coefficients in thin films and coatings, in highly transparent solids, and in liquids. Extension of this method to the investigation of nonlinear absorption phenomena is planned.

A NEW APPROACH TO PHOTOACOUSTIC RAMAN SPECTROSCOPY

In photoacoustic Raman spectroscopy[1] (PARS) two laser beams, one of which is tunable, pass collinearly through a gas sample enclosed in a spectrophone. One of the beams, referred to as the pump beam, can excite the molecules of the medium to virtual excited-electronic states. If the other beam, referred to as the Stokes beam, is tuned such that the frequency difference between the two lasers equals the frequency of a Raman-active vibrational mode of the molecules, it can produce stimulated Raman emission. The net result is a transfer of energy from the pump beam to the Stokes beam and a change in the vibrational state of the molecules involved in the Raman process. This vibrational energy is transferred to translational energy by collisions, and the resultant heating of the gas produces a pressure change which is detected with a microphone, as in ordinary photoacoustic spectroscopy. PARS has several attractive features distinguishing it from other coherent Raman processes: it has no threshold; it requires no phase matching; and, unlike coherent anti-Stokes Raman Scattering (CARS), the PARS signal is linearly proportional to the intensities of both the pump and the Stokes beams and also to the concentration of scattering molecules. Like CARS, it can be performed with light in the visible part of the spectrum where dye lasers serve as convenient sources of tunable coherent light, and it allows access to vibrational modes that are not infrared-active.

Among the problems encountered in PARS are the usual spurious background signal due to window heating (observed in ordinary photoacoustic spectroscopy) and the possibility of interference due to linear absorption of one of the laser beams due to (non-virtual) electronic transitions or vibrational overtones.

We propose to demonstrate some new techniques for PARS that alleviate the problems described above. A pulsed dye laser and a cw Kr^+ ion laser will provide the pump and Stokes beams, respectively. A spectrophone having a high Q acoustical resonance and designed to produce minimal back-

ground signal will be used.[2] An oscillator will be tuned to the acoustical resonant frequency of the spectrophone and used as a reference for a lock-in amplifier. The oscillator output will also be divided down to a subharmonic at which the dye laser is capable of firings.[3] If energy is being absorbed from the dye laser beam, then each pulse will produce ringing of the acoustical cavity. Since the dye laser is pulsed at a subharmonic of the cavity resonance, each pulse will reinforce the ringing left over from the previous pulse, which is still large due to the high Q, and a high pressure amplitude will develop at the resonant frequency of the spectrophone. This pressure amplitude will be detected by the microphone and lock-in amplifier. The signal thus detected could be due to the Raman process or could equally well be due to linear absorption of the dye laser beam or to window heating. The test of whether it is a Raman signal is whether it disappears when the ion laser beam is absent. Therefore, the ion laser beam is modulated at a low frequency which is used as a reference for a second lock-in. The output from the first, or high-frequency, lock-in is fed to the second lock-in, which picks out that portion of the output which is modulated at the ion laser chopping frequency. Since it is unlikely that the chopping of the ion laser beam will affect the linear absorption of the dye laser beam by the molecules or the windows, it can be concluded that this signal is due solely to the nonlinear interaction of the two laser beams caused by the Raman effect.

REFERENCES

1. J. J. Barrett and M. J. Berry, Appl. Phys. Lett. vol. 34, no. 144 (1979).

2. R. Gerlach and N. M. Amer, Appl. Phys. vol. 23, no. 319 (1980).

3. C. F. Dewey and J. H. Flint, Paper No. WC3, OSA Topical Meeting on Photoacoustic Spectroscopy, Ames, Iowa, Aug. 1-3, 1979.

DUMPING MECHANISMS IN ACOUSTICALLY RESONANT GASEOUS PHOTOACOUSTIC DETECTION

Photoacoustics has become important recently, largely because of the development of lasers. Resonant gaseous photoacoustics is important as a technique for the analysis of gases. An absorption spectrum can easily be obtained, or very small quantities of impurities can be readily detected.

One major unresolved question is, "What are the damping mechanisms that dominate the standing sound waves in a resonant photoacoustic cell?" It is vital that this be answered if the signal of resonant spectraphone (photoacoustic cell) is to be fully understood.

There are two categories of energy loss: volumetric losses and surface losses. Volumetric losses consist of what are called Stokes-Kirchhoff losses, radiation, diffusion effects, and molecular relaxational effects. Of these, only the molecular relaxational effects are significant. Surface losses are: (1) wave reflection losses due to the compliance of the walls, (2) scattering losses due to irregularities, (3) dissipation at the microphone, and (4) viscous and thermal losses at the cell boundaries. Each of these losses can be minimized by suitable construction of the cell.

The loss mechanisms can be experimentally verified by determining the Q of the cavity for a particular resonance.

$$Q = 2\pi \frac{\text{Total Energy in Cavity}}{\text{Energy Loss/Cycle}}$$

$$= \text{fm,n,p}/\Delta f\, 1/2 \text{ power}$$

where f is the resonance frequency.

The experiment is set up to accurately measure this Q for various pure "buffer gases" (i.e., optically transparent) mixed with 50 ppm of C_2H_4, the absorbing gas.

A CO_2 laser beam is opto-electronically modulated and travels axially down the center of a hollow stainless steel cavity filled with 50 ppm of ethylene in some pure buffer gas. The walls of the cavity were carefully polished to $\leq 1\mu$ and kept free of obstructions. The miniature microphone is mounted flush with the cylinder wall. The Q is measured by slowly scanning through a resonance. The data obtained is fitted, using a nonlinear least squares routine.

All the noble gases through Xenon have been investigated extensively at pressures from 10 torr to 1 atm. The final fitted Q's have little scatter and can be explained, considering only the viscous and thermal dissipation at the cell boundaires.

The diatomic and polyatomic gases investigated to date are H_2, N_2, CO_2, N_2O and SF_6. Concurrently, the theoretical work needed to explain the damping for these gases is in progress. However, the molecular relaxational model, in addition to viscous and thermal wall losses, adequately explains the damping in H_2 and is expected to be largely successful in the other gases.

Through this work, a tractable theory of damping in resonant gaseous photoacoustics will be achieved. This is important for the general knowledge of physics and of great practical importance in the field of photoacoustics.

A PROPOSAL FOR A NEW PHOTOTHERMAL DEFLECTION METHOD FOR PROBING SOLID SURFACES

In designing experimental apparatus to make photothermal measurements on solid surfaces in an ultra-high vacuum environment, there are numerous technological problems. Two of these problems are: (1) how to detect the PAS signal, and (2) how to make the experiment more surface specific.

One of the best known techniques for making optical measurements on solid surfaces is attuated total reflection (ATR) spectroscopy. This technique is illustrated in Figure 8. A glass prism is placed near the sample surface with a small gap ($\sim$.1-1 μm) separating them. If an optical

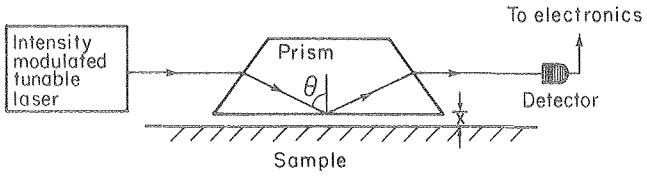

Fig. 8. Schematic of proposed experimental arrangement.

(XBL 812-162)

beam enters the prism as shown (Fig. 8), it would normally be totally reflected on the bottom surface of the prism. However, the presence of the sample surface close to the prism allows energy from the light beam to be coupled into the sample. An exact solution of Maxwell's equations for the coupled energy is straight forward. The amount of energy coupled into the sample, I, is

$$I \propto e^{-\alpha x} \qquad (1)$$

where x is the gap width and $\alpha = \frac{4\pi}{\lambda}\sqrt{h^2 \sin^2\theta - 1}$

where λ is the wavelength of the light, n is the index of refraction of the glass prism.

This technique not only makes any optical measurement more sensitive to the sample surface, it also can be used to detect the photothermal signal. Energy absorbed by the sample from an exciting beam of light, chopped at a frequency Ω, will generate acoustic phonons and thermal expansion. These will both cause the gap width, x, to be modulated at the chopping frequency, Ω. If a probe beam from a He - Ne laser is then passed through the prism in the ATR geometry, its transmitted intensity will be modulated at Ω. The calculation of the modulation of the transmission of the probe beam is straight forward. Because the gap width enters the equation exponentially, this can be a very sensitive technique for measuring small fluctuations of the gap. For the case of a silicon sample with a gap of 0.1 μm,

$$\frac{dT}{dx} \sim 5 \cdot 10^{-4} \ (1/\text{Å})$$

where T is the He Ne transmission. With phase sensitive detection, it should be possible to detect motions of 1Å or less.

AMORPHOUS PHOTOVOLTAIC SEMICONDUCTORS*

Amorphous photovoltaic semiconductors, such as hydrogenated amorphous silicon, hold promise for meeting DOE cost and efficiency guidelines for thin film solar cells prior to 1990. In order to achieve the higher conversion efficiencies required, it is necessary to better characterize the unique optical and transport properties of these materials. Photoacoustic and photothermal spectroscopies can be used to elucidate the optical and electronic properties of a-Si:H. Of particular interest is the investigation of the opti cal properties near the so-called bandgap. By combining luminescence studies, a full and accurate characterization of the de-excitation of these photo-excited amorphous semiconductors can be achieved.

Experiments investigating the optical properties of hydrogenated amorphous silicon are currently underway. The experiments are designed to yield new information on the details of the optical absorption, the nature of the bandgap, and the electronic properties which determine the photoconductivity.

OPTICAL PROPERTIES OF HYDROGENATED AMORPHOUS SILICON (a-Si:H)

Hydrogenated amorphous silicon is of great interest as a representative of a new class of disordered solids which can be doped and have a small density of states within the bandgap and a low intrinsic conductivity. Despite the interest in the physics of a-Si:H and its great potential for photovoltaic and vidicon applications, much of the important physics remains poorly understood. In particular, the density of states within the bandgap is not well measured, the mobility of the carriers as a function of excitation energy is unknown, and several competing models for the recombination of excited carriers remain experimentally untested.

One model for the carrier recombination is an electron that deforms the lattice and becomes trapped near a hole. The hole and the electron recombine radiatively, emitting sub-bandgap radiation (peaked at 1.3 eV). At higher temperatures, such as room temperatures, a non-radiative channel for de-excitation dominates the radiative channel. The alternative model proposes the existence of a "bump" in the density of states below the conduction band edge. At low temperatures, the electron is trapped in the sub-conduction band states and recombines radiatively with a hole. At higher temperatures, the sub-conduction band states are ionized to the conduction band, and the electron recombines non-radiatively.

N. Mott and W. Anderson have predicted that the mobility of the carriers as function of excitation energy predicted will exhibit a sharp decrease to zero due to the disorder of the material and the decreasing density of states within the gap. Renormalization theories also predict an abrupt decrease of the mobility as the excitation energy becomes smaller than the bandgap. This decrease has not been observed in a-SI:H; and, in fact, some workers believe that the mobility does not show a decrease until far into the gap.

Finally, the effect of the preparation conditions on the density of states, optical properties, and the mobility are not well characterized. It is known that the concentration of hydrogen within the film, the deposition rate, the substrate temperature, and the film thermal history affect the

*This work was supported by the Assistant Secretary for Conservation and Solar Energy, Office of Solar Energy, Photovoltaic Energy Systems Division, U.S. Department of Energy under Contract No. W-7405-ENG-48.

bandgap as well as the mobility of the carriers. Exactly how these parameters affect the film awaits further understanding of the carrier transport and recombination mechanisms.

We have begun a series of measurements of the absorption of the films at and below the bandgap using photothermal deflection techniques. This is an ideal technique because the films cannot be thickened, and the subgap absorption is small. We have succeeded in measuring an $\alpha\ell$ of 5×10^{-4} at photon energies of 0.6 eV.

Because the absorption is proportional to the joint density of states, if the matrix elements are energy independent, the "bump" in the density of states predicted by one of the recombination models should give rise to a shoulder in the absorption spectra below the absorption edge. The model, which hypothesizes that electron deforms the lattice, predicts no such "shoulder." Therefore, we should be able to decide between the two models. Additionally, by comparing the observed absorption to that predicted by various models for the density of states, we may be able to eliminate some models.

If we compare the absorption data with photoconductivity data, we can measure the mobility-lifetime product as a function of excitation energy. Finally, by performing such experiments for samples prepared under different deposition conditions, we may shed some light on the connection between the deposition parameters and the properties of the films.

INVESTIGATION OF CARRIER DRIFT MOBILITY BY PHOTOTHERMAL DEFLECTION SPECTROSCOPY

Reported values of the drift mobility of the carriers in hydrogenated amorphous silicon have varied by as much as two orders of magnitude, due in part to the indirect nature of the techniques employed. We initiated a set of experiments which employ a very different technique and which, in principle, should yield a more direct determination. Briefly, electrodes are deposited on a hydrogenated amorphous Si film which is then placed in a fluid (in this case, CCl_4). An alternating electric field would spatially modulate a conduction band population in the film. A chopped Ar^+ laser beam generates the conduction band population. The heat of recombination flows from the location of the carrier population into the film and the surrounding fluid, producing a local gradient in the index of refraction, n, which follows the field. A second, sub-bandgap probe laser beam will then be deflected by the gradient of the index of refraction that is synchronous both with the Ar^+ laser beam, which creates the gradient, and the electric field, which spatially displaces the gradient. The deflection is detected with a position sensor placed some distance from the film. A two lock-in detection scheme discriminates in favor of deflections arising from both sources together.

From independent measurement of τ, the carrier movement, $l = \mu E \tau$ yields the mobility. This experiment, which was begun in the summer of 1980, is continuing.

LIQUID CRYSTAL RESEARCH*

The liquid-crystalline state of matter is characterized by a spontaneous anisotropic order and by fluidity. The anisotropic order leads to anisotropy in the physical properties of the medium, and the fluidity makes it easily susceptible to external perturbations in the form of electric or magnetic fields, temperature, or pressure. In addition, we have demonstrated that certain gaseous organic pollutants change the liquid-crystalline structure. This change, which is readily detectable, is the basis for an inexpensive and sensitive (10^{-6}) personal dosimeter for some organic pollutants. Once their physical properties are well understood, the class of liquid crystals known as lyotropics offers the potential for employing such a material for the efficient recovery of oil from abandoned wells and from oil shale.

PHYSICAL PROPERTIES OF LIQUID-CRYSTALLINE MONOLAYERS

Lyotropic liquid-crystalline monolayers are interesting for several reasons. First, not unlike other 2-d systems but unlike one-dimensional systems, these monolayers exhibit a variety of phases; many of these phases are similar to those observed in three dimensions. Also, these 2-d systems may have important technological applications in such diverse fields as oil recovery, catalysis, electronics, and liquid crystal displays. Additionally, 2-d systems are interesting in their own right and are not yet well characterized, either experimentally or theoretically. Furthermore, they are of unique biological importance.

The particular 2-d system we are investigating consists of a high-purity monolayer of amphiphillic lecithin molecules at a water-aliphatic hydrocarbon liquid interface. This system exhibits interesting phase behavior at temperatures slightly above room temperature because the submonolayer is compressed toward a close-packed state. To date, most work on this type of system has been conducted on air-water interfaces where complex motion of the "tails" obscures the results. The oil-water interface used places the tails in their natural milieu.

We have chosen to investigate this system using the non-perturbing technique of light scattering. Scattering from the monolayer molecules themselves is very small. However, the presence of the monolayer causes reduction of the interfacial tension and greatly alters the behavior of small wavelength capillary waves at the liquid-monolayer-liquid interface. In thermal equilibrium, r.m.s. fluctuations of the interface are on the order of a few angstroms. These fluctuations consist of the superposition of a large number of traveling wave frequencies, ω, and wavelengths,

*This work was supported by the Assistant Secretary for Environment, Office of Health and Environmental Research, Pollutant Characterization and Safety Research Division of the U.S. Department of Energy under Contract No. W-7405-ENG-48.

q. Any given wave of fixed q will act somewhat like a moving diffraction grating and will cause part of the laser beam to be scattered into an angle determined by q with frequency shifts of $\pm \omega$. Thus, the scattering is caused by a change in index of refraction between the two bulk liquids. Typical values are $q \sim 350\ cm^{-1}$ and $\omega \sim 6 \times 10^4\ sec^{-1}$. In this experiment, the laser beam enters and leaves the upper non-polar liquid through a coupling prism at right angles to the beam (Fig. 9). A small fraction of this beam is scattered, relative to the reflected beam, into angles $\lesssim 1$ degree. Some light is also elastically scattered into small angles by the liquids and optical components. The beam then leaves the system by a path similar to that by which it entered. Next, a precision small angle rotation is made on the beam, causing the main beam to go off axis and allowing light scattered by the negative of this angle to enter a small pinhole and finally a photomultiplier. Here, the elastically and inelastically scattered light beats together on the photocathode, generating a photocurrent containing the difference or ripple frequency. A real-time digital autocorrelator and microcomputer determines the frequency and the damping coefficient from the time correlation function.

To obtain the interfacial tension from ω and q, an accurate hydrodynamic theory of the fluctuation-driven ripples is needed. As an illustration, the dispersion relation for harmonic waves on the clear surface of a single liquid is

$$\omega^2 = \gamma q^3/\rho + g\,q$$

where γ (T) = surface tension at a given temperature

ρ = liquid mass density (3-d)

g = acceleration due to gravity

Since we investigate only very small q values, we may ignore the gravity term and a measurement of ρ, w, and q will give the surface tension in this simple case. The actual experimental situation is complicated by a second liquid, bulk (3-d) liquid shear viscosities, the visco-elastic constants of the 2-d monolayer, and the fact that not all waves are harmonic. Therefore, we have extended the anharmonic theory of fluctuation-driven ripples of a single fluid to our system. The predicted power spectra can be fit to the Fourier transformer of the measured time correlation function. To be discussed later is the fact that hydrodynamics also give the form of the power spectra for "longitudinal" waves in which the monolayer molecules move in the plane of its interface. A schematic of experimental equipment is shown in Figure 10.

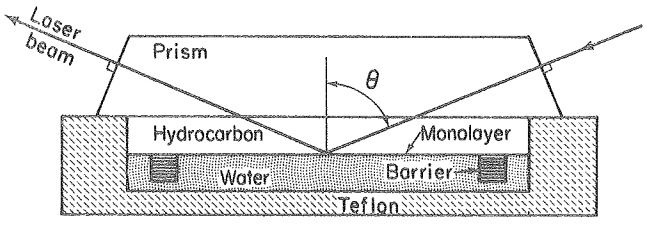

Fig. 9. Details of the scattering configuration (side view). (XBL 812-160)

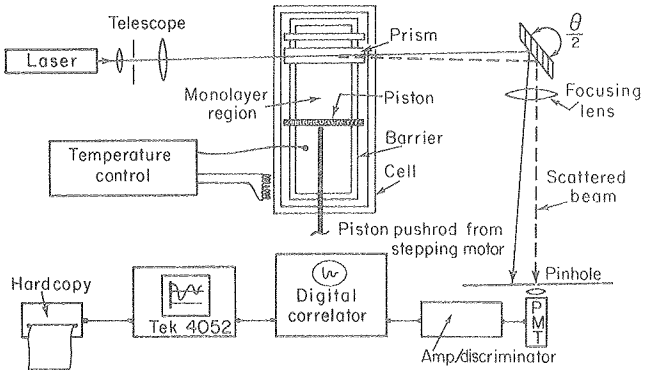

Fig. 10. Schematic of experimental equipment (top view). (XBL 812-161)

Measurements already obtained show three interesting regions along a 2-d isotherm. At low concentrations, there seems to be a single fluid-like phase and, at high concentration, a much more rigid solid-like phase. Between these two phases is an intermediate region where the isotherm has a very slight or zero slope. This region, which begins by a rather abrupt change in slope from the fluid-like region, seems to smoothly enter the solid-like region. These results are preliminary in nature.

There are several theoretical models for these 2-d phases. Models specifically dealing with amphiphillic monnolayer usually treat the transition region as being the result of the "melting" of the molecules' hydrocarbon tails to a more random state. One would predict a first order phase transition with a coexistence region for this type of model. A general theory of two stage melting in two dimensions, recently developed by Halperin and Nelson, predicts a solid with algebraic decay of translational order and long range orientational order. At high temperatures, an unbending of dislocations could allow the system to enter a "hexatic liquid crystal" phase with a reduction in both types of order. Even higher temperatures would result in an isotropic 2-d fluid with exponential decay of all order.

The Halperin-Nelson theory makes dramatic predictions for the dynamic properties of such a system. The 2-d shear viscosity behavior would provide a clear test of this model if it could be determined accurately. Our light scattering measurement provides some sensitivity to the 2-d viscosity of the monolayer. Much greater sensitivity would be provided by scattering due to the "longitudinal" waves mentioned earlier. This is a possible direction for future work. At present, we are concentrating on clean, unambiguous data on the equilibrium properties of the system. These measurements should give us the 2-d phase diagram which is badly needed. Once this is accomplished, accurate measurements of dynamic properties, such as viscosity and mass diffusion, can be attempted.

OPTICAL DETERMINATION OF SMECTIC LAYER SPACING IN FREELY SUSPENDED LIQUID-CRYSTALLINE FILMS†

The accurate determination of smectic layer spacing is of technological interest. Complex methods exist for accomplishing this task. We have employed a simple optical approach to deduce the layer spacing of smectic A thin films ($2 \leq N \leq 15$). Since these freely suspended films are much thinner than optical wavelengths, one can make use of optical interference effects to measure smectic layer spacings. In the case of a light beam incident on a thin uniform[1] slab of material, the reflectivity coefficients for electric fields in ($R_\parallel$) and perpendicular to ($R_\perp$) the plane of incidence are given by[2]

$$R_\parallel = \frac{\left(n_\parallel^2 \cos^2 i - \cos^2 r_\parallel\right)^2 \sin^2 a_\parallel}{4n_\parallel^2 \cos^2 i \cos^2 r_\parallel + \left(n_\parallel^2 \cos^2 i - \cos^2 r_\parallel\right)^2 \sin^2 a_\parallel} \qquad (1)$$

$$R_\perp = \frac{\left(\cos^2 i - n_\perp^2 \cos^2 r_\perp\right)^2 \sin^2 a_\perp}{4n_\perp^2 \cos^2 i \cos^2 r_\perp + \left(\cos^2 i - n_\perp^2 \cos^2 r_\perp\right)^2 \sin^2 a_\perp} \qquad (2)$$

where: i = angle of incidence

$r_\parallel$ ($r_\perp$) = angle of refraction for the parallel (perpendicular) mode

$n_\parallel$ ($n_\perp$) = index of refraction for the parallel (perpendicular) mode

$a_\parallel = n_\parallel\ k\ h \cos r_\parallel$

$a_\perp = n_\perp\ k\ h \cos r_\perp$

k = wavevector of light

h = thickness of film

The smectic A phase is birefringent and the optic axis lies perpendicular to the plane of the film and therefore in the plane of incidence (see Fig. 11). Therefore, $n_\perp$ is independent of i and is equal to n_o, the ordinary component of the refractive index. However, for light polarized in the plane of incidence (parallel mode), $n_\parallel$ is given by the usual formulae

$$n_\parallel = \left[\frac{\sin^2 r_\parallel}{n_\varepsilon^2} + \frac{\cos^2 r_\parallel}{n_o^2}\right]^{-1/2} \qquad (3)$$

and $\sin r_\parallel = \dfrac{\sin i}{n_\parallel}$, (4)

which easily simplify to yield a transcendental equation in the variable $n_\parallel$. Here n_ε is the extraordinary component of the refractive index. In principle, three independent measurements of $R_\parallel$ at three different angles i would yield n_o, n_ε, and the film thickness h. Such a measurement, in addition to yielding the film thickness, and hence layer spacing for a film of N layers, would provide useful information about the density of the film, through the symmetric component of the dielectric tensor. It would also provide information about the orientational order through the asymmetric component of the dielectric tensor. Nevertheless, small errors in such quantities as $R_\parallel$ and uncertainties in i strongly propagate in this technique, creating errors in the quantities of interest sufficiently large to render this measurement meaningless.

We have consequently opted for a somewhat less ambitious, though nevertheless interesting,

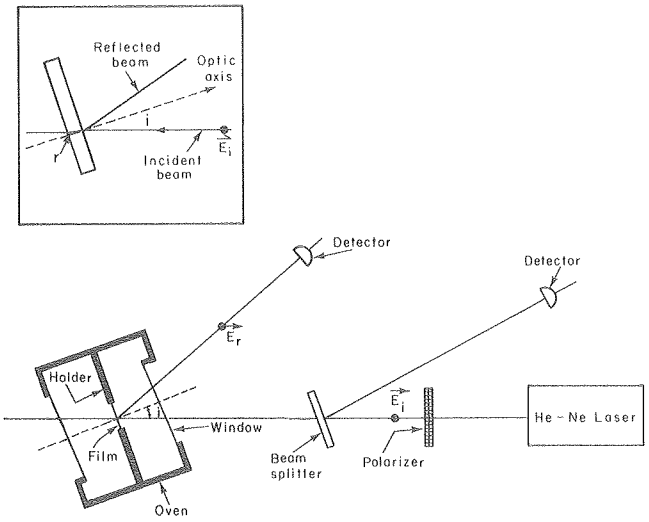

Fig. 11. Schematic of experimental arrangement. (XBL 7910-4520)

†Complete version of this work appeared in Appl. Phys. Lett. vol. 36, 432 (1980).

measurement. One measurement of $R_{\parallel}$ at a given angle yields a surface in (h, n_o, n_ε) space [Eq. (1)]; on the other hand, a measurement of $R_{\perp}$ at some angle i yields a line h vs. n_o. Therefore, although we cannot extract absolute values of h and n_o, we can nevertheless gain some insight as to their behavior in thin films.

Three materials are investigated: octyloxy cyanobiphenyl (80CB) butyloxybenzylidene octylaniline (40.8), and cyanobenzylidine octyloxyaniline (CBOOA). The experimental arrangement is shown in Figure 11.

Thirty to forty films are drawn at a given temperature for each material studied. The measured reflectivities are quantized, developing well-defined values corresponding to the number, N, of smectic layers; the scatter in data around any given value of $R_{\perp}$ is generally less than 1%. For very thin films (N 15), Equation 2 reduces to $R_{\perp} \propto h^2$. Assuming that $h = a_o N$, where a_o is a constant layer spacing, one can associate a value of N with each $R_{\perp}$ such that $R_{\perp} \propto a_o^2 N^2$. We also assume that the index of refraction n_o is constant and independent of film thickness. Therefore, from Equation (2), we calculate a film thickness for each measured $R_{\perp}$ and N. In Figure 12a, we plot h vs. N, assuming $n_o = 1.50$, the bulk value for 80CB at T = 67.3°C. Performing a least squares fit to the function $h = a_o N + b$, we obtain $a = 31.1 \pm 0.2$, $b = -1.4$, and an rms error of 2.2. The very small negative intercept is characteristic of all our results. Although it may arise from real physical effects, such as slightly thinned outer layers because of the asymmetric environment near the surface, it can also be due to a changing value of n_o, which is a function of N.

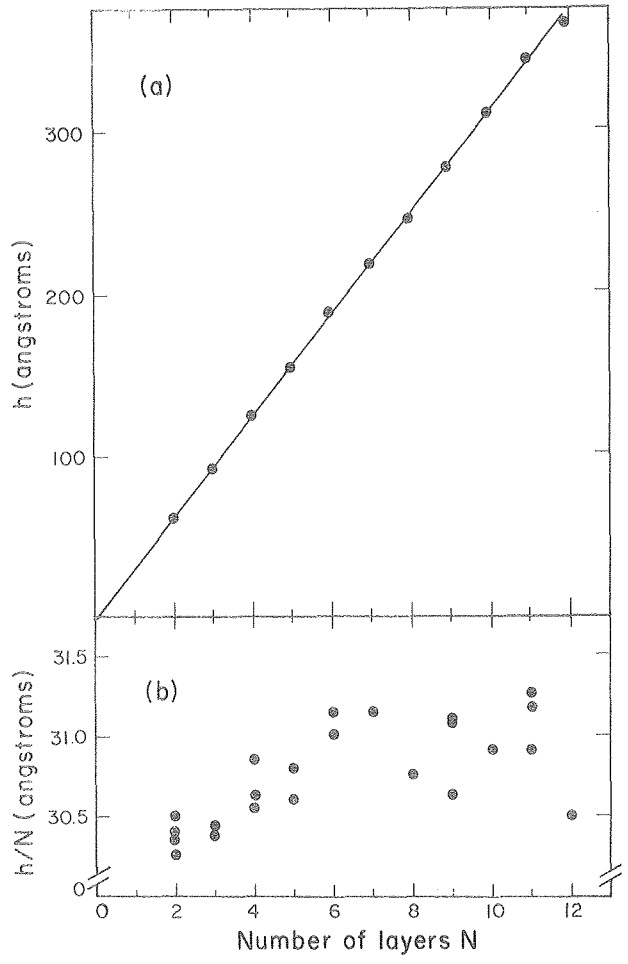

Fig. 12. (a) Film thickness vs. N in 80CB at 65.5° C, assuming n = 1.50. Line is least squares fit to dta points. Error° bars are approximately ± 1%.

(b) h/N vs. N for some material. (XBL 7910-4522)

In Figures 13a, b, and c, we plot layer spacing vs n_o for the materials 80CB, 40.8 and CBOOA respectively. We have assumed that n_o is constant as a function of N and, therefore, that the layer spacing shown is the slope of the h vs. N line (Fig. 12a). If one assumes, however, that n_o is N-dependent (Fig. 12b) and that a_o is simply h/N, values of a_o would be reduced by 0.1 to 0.2 Å in thicker films from those reported in Fig. 13, for a constant n_o. In thinner films, the correction would be slightly greater. Since the error bars for a_o are ± 0.5 Å, these corrections fall within experimental error.

We have also investigated the temperature dependence of the layer spacing. For 80CB and 40.8 there appears to be no systematic temperature-dependent behavior of h vs. N_o in the films. In CBOOA, however, there appears to be a weak but systematic increase in a_o as a function of temperature. The data shown in Figure 13c are for T = 82.3° C. Assuming a fixed n_o, a_o decreases by approximately 0.2 Å at T = 74.5° C and increases from that shown by 0.2 Å at T = 85.3° C. It is interesting to note that this is the first reported case of a smectic A film existing at temperatures which would normally be nematic in bulk.

In Figure 13, asterisks show the approximate bulk behavior in the smectic A phase at T = 64° C for 80CB, T = 60° C in 40.8, and T = 80° C in CBOOA. Although the bulk data lie very close to the a_o vs. n_o lines, the measured values of a_o are consistently smaller than their corresponding bulk values, assuming n_o is identical in film and bulk. Such an effect might arise from an asymmetric surface potential or the smeared-out nature of the film's surface. However, one can also view the data from the standpoint of a_o being the same in both bulk and films, with n_o in films being smaller than in bulk. Such an effect can arise from a decreased density in films because films tend to maintain the chemical potential of the bulk reservoir in the presence of a surface tension.

REFERENCES

1. Molecular times are much faster than detector response times; the detector therefore integrates over thermal motions, resulting in a uniformly appearing slab, except perhaps near the surfaces.

2. M. Born and E. Wolf, Principles of Optics, Pergamon Press, Oxford (1975).

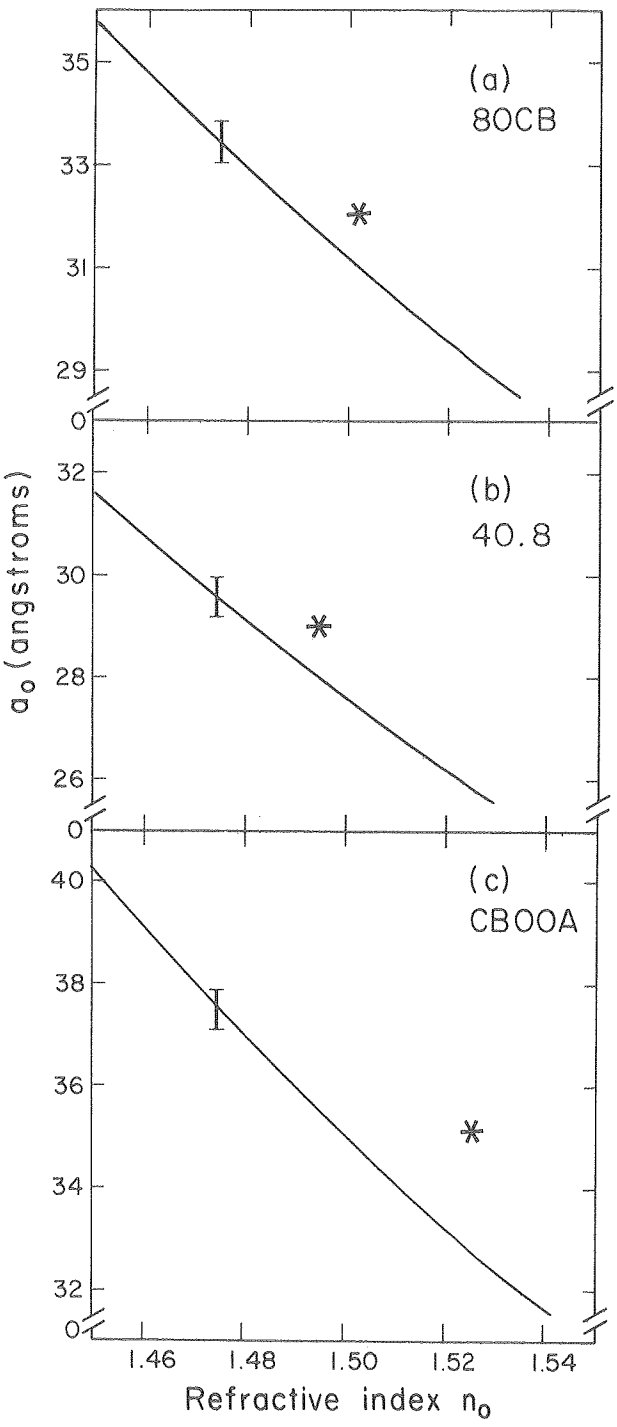

Fig 13. Layer spacing obtained in Fig. 12 vs. ordinary refractive index, n_o, for three materials. Error bars are as shown. Asterisks represent bulk data, where values of a_o are obtained from x-ray experiments. (XBL 7913-4521)

NOVEL LASER SYSTEMS*

Our research activities encountered experimental conditions which require the development of novel approaches to laser technology. An example of such a case is the simple waveguide CO_2/N_2O laser described in the 1978 Annual Report and which has been published in Reviews of Scientific Instruments. During FY 1980, we conceived a novel method for obtaining ultrashort pulses from cw dye lasers. This summary briefly describes this laser and a method for monitoring such ultrashort pulses in "real-time".

RECIPROCAL PASSIVE MODE-LOCKING OF A CW DYE LASER AND THE ION PUMP LASER†

With the advent of synchronous pumping, mode-locked cw dye lasers have become an important tool for performing time-resolved spectroscopy. In such a scheme, an acousto-optically mode-locked cw ion laser (pulse width of $\sim$ 100 pSec) externally pumps a dye laser whose cavity length is matched to the cavity length of the pump laser. When the lengths of the two cavities are optimally matched to within a few μm, picosecond pulses are generated. Such pulses have considerably higher average power and wider tuning range than those obtained from cw-pumped passively mode-locked dye laser systems.

We present here preliminary results of the reciprocal passive mode-locking of the 5145 Å line of an Ar^+ laser by an intracavity Rhodamine 6G (R6G) dye laser. This mode-locked line, in turn, synchronously mode-locks the dye-laser-generating, tunable, ultrashort pulses of duration and average power comparable to those obtained from synchronously mode-locked systems. Our approach, therefore, eliminates the need for actively mode-locking the pump laser with an acousto-optic modulator driven by the amplified output of a stable oscillator. Furthermore, we observe that the pulse width appears not to be too critically dependent on the mismatch of the two cavities.

Fig. (14) shows a schematic of this mode-locking arrangement. The Ar^+ laser cavity is extended, in a folded configuration, to include the broadband high reflecting mirrors, M_1 and M_2 (10 cm radius of curvature R). The dye jet stream is placed at the focus of the mirrors at Brewster's angle. The cavity is completed through prism P and a flat high reflecting mirror M_3. The dye laser beam, which has M_1, M_2, and P in common with the argon beam, is dispersed by the prism P and propagates to a partially transmitting end mirror M_5 ($R = \infty$, transmission T=3%).

In this intracavity pumped configuration, R6G acts as a saturable absorber of the 5145 Å line. However, its relaxation time, $\sim$ 6 n Sec, is not short enough to induce mode-locking. When M_5 is misaligned such that R6G is not lasing, it is observed that the Ar^+ intracavity intensity is strongly modulated but not completely mode-locked. On the other hand, when M_5 is aligned to allow R6G to lase, short-pulsed operation of the 5145 Å

*This work was supported by the Assistant Secretary for Environment, Office of Health and Environmental Research, Pollutant Characterization and Safety Research Division of the U.S. Department of Energy under Contract No. W-7405-ENG-48.

†Complete version accepted for publication in Optics Lett., vol. 6 no. 67 (1981).

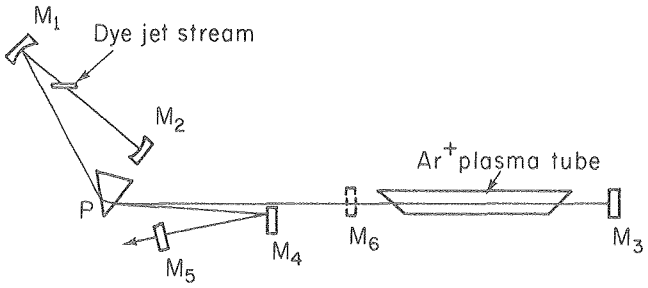

Fig. 14. Reciprocal mode-locking scheme. M_1 and M_2: broadband high reflectors (r = 10 cm). M_3: R6G high reflector (R = ∞). M_4: Ar^+ broadband high reflector (R = ∞). M_5: R6G partial transmitter (R = ∞). M_6: Ar^+ output coupler (removed after initial alignment, see text). (XBL 8010-2264)

line is obtained, as coarsely monitored with a fast photodiode and a sampling oscilloscope. This occurs when the cavity length of the dye laser is optimally adjusted by the translation of M_5 with a differential micrometer to a position approximately equal to, or one-half of, the cavity length of the Ar^+ laser. The passive mode-locking of the Ar^+ laser is the result of the effective shortening of the relaxation time of the saturated dye absorption, caused by the formation of a dye laser pulse at the trailing edge of the Ar^+ laser pulse. This stimulates a rapid depletion of the excited S_1 state of the dye. The dye laser pulses, in turn, will also be ultrashort, being synchronously pumped by the mode-locked Ar^+ laser pulses.

A typical autocorrelation trace of pulses at λ = 5700 Å is shown in Fig. (15). Assuming a $sech^2$ pulse shape, the measured pulse-width is 11 pSec. Similar pulses were observed over a wavelength range of 5650 Å - 5950 Å, with a typical average power output of ∿ 80 mW. In general, the pulses have amplitude substructure as evidenced by the 3 : 2 : 1 contrast ratio. The typical FWHM bandwidth of such pulses was ∿ 4 Å. Shorter pulses, without substructure, were also observed with a 3 : 1 contrast ratio, but these pulses are not easily reproduced, even after the introduction of an iris in the dye laser cavity.

Although the presently generated pulse widths are somewhat longer than those obtained from conventional synchronously-pumped mode-locked dye lasers, our approach has several advantages. First, the active mode-locking of the pump laser is eliminated. Second, our preliminary results indicate that the optimum pulse duration may not be critically dependent on the cavity mismatch parameter. Finally, because mode-locking was achieved at small values of linear cavity losses, cavity dumping techniques can be readily incorporated into this system.

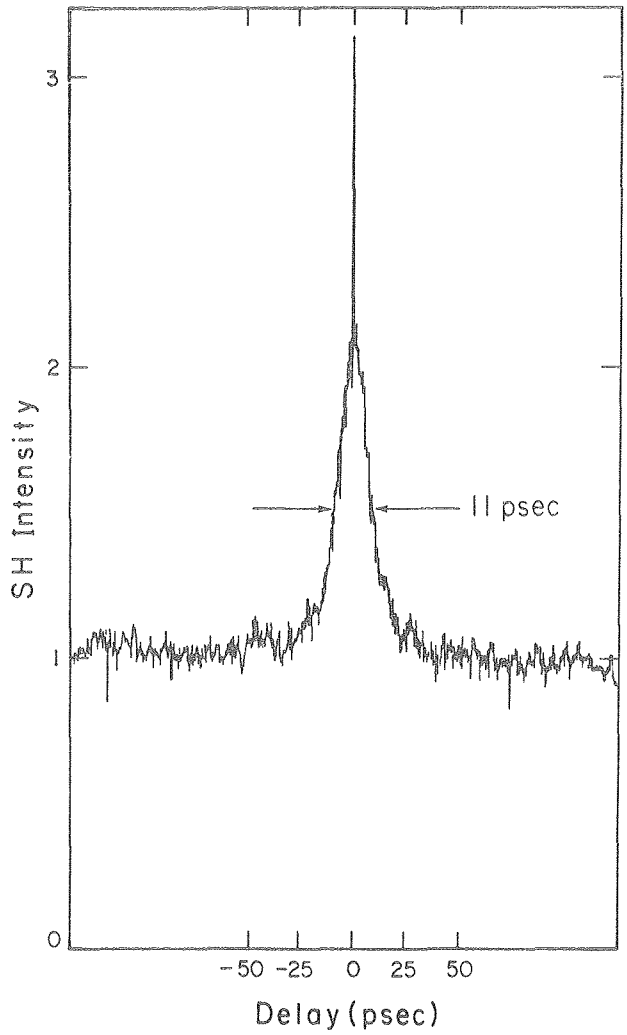

Fig. 15. Intensity autocorrelation trace (with background, $sech^2$ pulse shape) of a typical dye pulse. (XBL 8010-2267)

A SCHEME FOR CONTINUOUS MONITORING OF PICOSECOND LASER PULSES IN REAL-TIME†

Although the standard method for measuring the width of the pulses produced by these laser systems is the well known second harmonic (SHG) autocorrelation technique, useful autocorrelation traces require minutes to obtain. It is therefore desirable to devise methods which enable the continuous monitoring of the temporal characteristics of these pulses in "real time". One approach involves the rapid introduction of a periodically varying time delay in one arm of the Michelson interferometer (MI) used in conventional second harmonic generation autocorrelators.

This summary describes a simple yet precise method for the introduction of a periodic time delay to a train of picosecond laser pulses. It enables the high resolution display of the auto-

†Complete version of this work appeared in Optics Comm. vol. 36, p. 406 (1981).

correlation function of picosecond pulses continuously on an oscilloscope. This method is highly linear over a wide scanning range ($\geq$ 150 psec) and is dispersion-free.

The rapid introduction of a linear periodic time delay is achieved by incorporating in one arm of the Michelson interferometer a pair of parallel mirrors mounted on the two ends of a shaft rotating at a constant angular frequency f (Fig. 16). Thus, after being equally split by the beam splitter, one half of the incoming train of picosecond pulses is incident on mirror M_1 and is reflected to mirror M_2, from which it is transmitted in a direction parallel to that of the original direction. Following a rotation of the shaft by an angle θ, this beam traverses a different path (i.e., is delayed) and is transmitted with a certain displacement while remaining parallel to the direction of incidence. The transmitted beam is normally incident on a stationary mirror M_3, from which it is retroreflected, retracing the incident beam in the opposite direction.

In the other arm of the MI, a stationary mirror M_4 (mounted on a translation stage) retroreflects the other half of the incoming train of pulses; and the two reflected beams from mirrors M_3 and M_4 are recombined collinearly at the beam splitter. The combined beam is focused onto an angle-phase-matched nonlinear crystal, and the generated second harmonic is detected by a photomultiplier, as in conventional autocorrelators. In our scheme, however, the photomultiplier output is the input to a high impedance oscilloscope. The time-base of the oscilloscope is triggered by the output of the photodiode PD which is placed between M_2 and M_3 in such a way that it intercepts a portion of the beam before it is incident on M_2. As shall be seen in the next section, the rotation of the parallel pair of mirrors, M_1 and M_2, results in a linear variation of delay with time. Therefore, the oscilloscope directly displays the second order intensity autocorrelation, with background, of the incoming train of pulses. To properly position the autocorrelation trace, one translates mirror M_4 until a peak occurs at the center of the scan range on the oscilloscope screen. The calibration of the oscilloscope in terms of delay is done by measuring the displacement of the autocorrelation peak on the screen for a given translation of M_4.

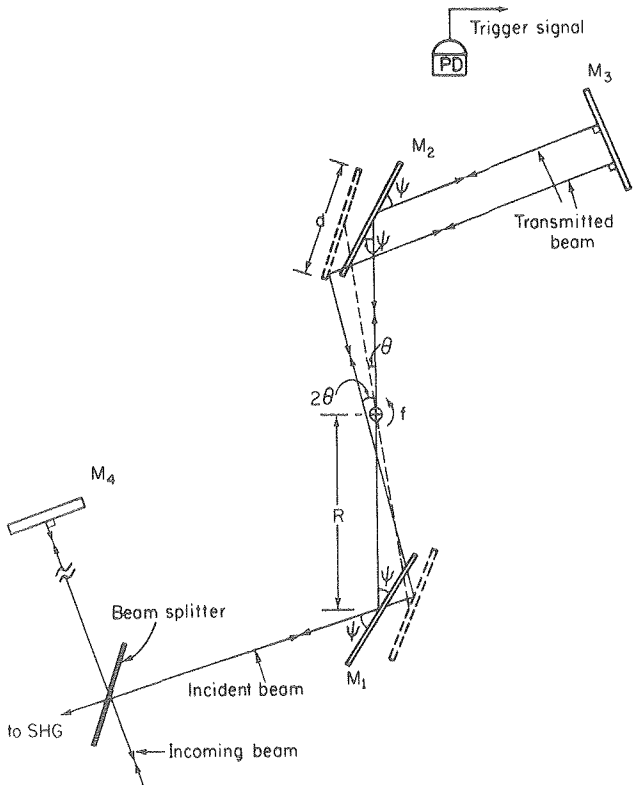

Fig. 16. The rapid-scanning Michelson interferometer part of the SGH autocorrelator. R is the radius of the rotating shaft, d is the mirror diameter, and ψ is the angle of mirror orientation with respect to the incident beam. Dashed lines represent the shaft and mirrors after a rotation by an angle θ. PD is the photodiode used to trigger the oscilloscope. (XBL 8010-2270)

Figure 17 shows the intensity autocorrelation trace, with background, for a cw train of incompletely mode-locked R6G dye laser pulses, as displayed on an oscilloscope using the above described method. As can be seen from the figure, the coherence spike and the contrast ratio of 3:2:1 are clearly observed.

In principle, the time resolution of this autocorrelator is set by the second harmonic generation process itself. This is true as long as the rise time of the detection and displays parts of the autocorrelator are sufficiently fast.

PLANNED ACTIVITIES FOR FY 1981

Future Directions

In the area of laser photoacoustic and photothermal detection, work will continue in developing ultra-sensitive multiparameter molecular detectors for the characterization of gaseous trace contaminants, particularly those associated with synfuels. Emphasis will be placed on in situ

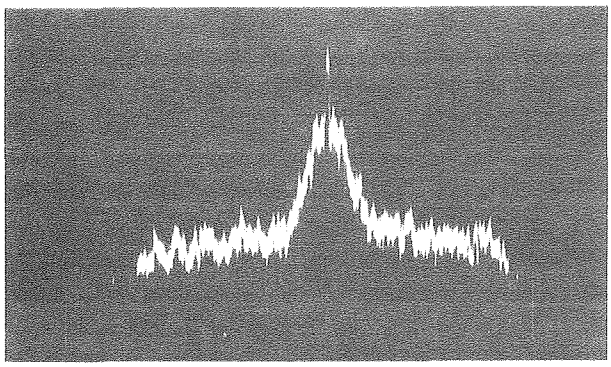

Fig. 17. Rapidly scanned, 2nd-order-intensity, autocorrelation trace of a cw train of ultrashort dye laser pulses. Horizontal scale is 500 μsec/division. Vertical scale is 40 mV/division. (XBL 8011-12725)

and remote sensing schemes. We plan to extend opto-acoustic and photo thermal detection to water pollutants, with specific emphasis on nitrates, sulphates, and photo thermal and organic contaminants. The elemental detection and analysis by tunable laser photoacoustic spectroscopy is planned. In collaboration with the Atmospheric Aerosol Research Group at LBL, we will continue the investigation of optical properties of carbonaceous particulates.

In studying amorphous photovoltaics, our primary effort will continue to center on the physics of those processes governing conversion efficiencies of solar cells made of these amorphous semiconductors. The optical characterization of hydrogenated and flourinated amorphous silicon will continue with particular emphasis placed on the nature of gap states. Experiments, initiated this summer to investigate the mobility of photogenerated carriers, will continue; and time-resolved studies of the de-excitation mechanisms of photoexcited amorphous silicon will be conducted. Other amorphous photovoltaics, e.g., amorphous gallium arsenide, will be studied.

Various potential applications of liquid crystals will continue to be explored. Optimization and comparison of ferro-nematic and ferro-cholesteric dose-integrating magnetometers will resume. Work on gaseous organic detectors will continue to investigate the fundamental mechanism responsible for the observed effect, and sensitizers will be incorporated in the liquid crystal detector to adjust the concentration threshold. In the study of lyotropic monolayers, work will continue on the oil-water interface case, and the emulsification and vesicle formation will be investigated. Finally, the activities in the area of laser development will focus on further narrowing the pulsewidth of our "reciprocal mode-locking" scheme to the subpicosecond regime.

MICROPROCESSOR CONTROLLED ANODIC STRIPPING VOLTAMETER FOR TRACE METALS ANALYSIS IN WATER*

R. Clem, F. Park, F. Kirsten, S. Phillips, and E. Binnall

INTRODUCTION

Trace metals in public drinking water supplies are of special concern because of their potential long-term harmful effects after being ingested.[1,2] Water supply resources for municipalities vary in both the type and concentration of dissolved metals; in untreated water these concentrations are generally significantly lower than the EPA Interim Primary Drinking Water Standards.[3,4] However, chemicals used in water treatment and containing traces of metals as impurities may introduce these metals to water at the treatment plant. Another potential source of metals is corrosion and dissolution of metallic piping or tank interiors through which the treated water passes or is stored prior to ingestion. Thus, there is a need to measure the concentration of dissolved metals at the user tap where the water is actually ingested by a household.[4]

While a number of methods are available for measuring trace metals in drinking water,[1] the method described herein was selected because anodic stripping voltametry (ASV) offers a number of advantages including: (1) capability for simultaneous analyses of more than one metal; (2) sensitivity to concentrations levels less than 1 μg/L; (3) portability of instrumentation; (4) capability for metal speciation at ambient concentrations; (5) ease of automation; and (6) rapid analyses at a relatively low cost.

This report describes the ASV instrument system constructed by LBL; calibration of the instrument with known metal concentrations; and results of analyses of tapwater in Seattle, Washington, and Berkeley, California. Selected background information is given on the anodic stripping electrochemistry of Cd, Pb, and Cu; the ASV method using mercury thin films plated onto graphite electrodes; and the instrumentation electronics.

ANODIC STRIPPNG VOLTAMETRY AT MERCURY FILM ELECTRODES

Anodic stripping is applied to the analysis of mercury soluble metals, such as cadmium and lead, using thin films formed by the deposition of mercury onto carbon electrodes.[5] The Hg is co-deposited with the metals (Cd,Pb,Cu) being analyzed.

The first step involves electroplating during which the metals being determined are concentrated within the Hg film. This deposition step is not exhaustive (non-stoichiometric). The applied potential is stepped to a sufficiently negative value so that the electrodeposition rate is limited only by the rate of mass transfer of the dissolved metals from the bulk of the solution to the electrode surface. The solution is stirred by rotating the cell to enhance mass transfer. The plated metals being analyzed establish a concentration gradient within the Hg film whereby the concentration of metal at the electrode-solution inter-

*This work was supported by Drinking Water Research Division, Municipal Environmental Research Laboratory, Office of Research and Development, U.S. Environmental Protection Agency, under Interagency Contract No. EPA-790-X-0507 and by the U.S. Department of Energy under Contract No. W-7405-ENG-48.

face is larger than that toward the interior of the electrode.

After a set time, such as 5-10 minutes, stirring is stopped, and the solution becomes quiet. During this quiescent period, the concentration gradient within the Hg film is essentially eliminated because deposition is almost negligible, and the plated metals diffuse through the film from regions of high concentrations to lower concentrations.

The third step is anodic stripping of the metals from the amalgam by application of a linearly increasing positive potential. At potentials near the Nernstian value for a particular metal, the metal begins to dissolve (strip) giving rise to typically peak-shaped curves at more positive potentials. A peak is obtained for each metal, thus a charge-voltage curve can consist of more than one peak. Usually, this peak height is measured and related to the metal concentration in the solution via calibration data. Peak areas have also been measured.

INSTRUMENT SYSTEM COMPONENTS

The ASV system constructed here was designed to automate settings for the analytical procedure, to acquire data relating peak height to metal concentration in water samples, and to store data from the analysis of tap water for subsequent calculations. The system is comprised mainly of the following: a rotating cell containing the water sample, electrodes and inlet for the sparge gas; the electronic controller for plating and stripping; and a pen recorder or magnetic tape for data storage and calculation (Fig. 1). The functions of these four major components described in Table 1 are discussed below.

Rotating cell

A cylindrically shaped rotating cell machined from Lucite was used to provide both quick oxygen removal during the sparging step and a high rate of metal preconcentration during the metal deposition. Only 60 seconds is required for effective oxygen removal. Quick oxygen sparging is important in reducing the time required for an analysis.[5] The solution volume used was generally 15 mL.

During oxygen sparging, the cell containing the 15 mL of solution is rotated automatically in a clockwise direction for 0.9 seconds; a counterclockwise pulse is then imparted for a duration of 0.1 seconds. Under these conditions, the dissolved oxygen concentration is lowered until the background current due to oxygen reduction does not interfere with the analysis procedure.

Nitrogen or other inert gas, such as carbon dioxide, is introduced near the bottom of the cell through the bottom of the electrode holder at a rate of ∿5 L/min to effect sparging. At the conclusion of the 60-second sparging period, the microprocessor stops cell rotation, and the solution drains completely to the floor of the cell because a Lucite surface is not wetted by water. Then the agitation (stirring) period is begun; during this time, amalgam is accumulated in the preconcentration step. A low flow rate of nitro-

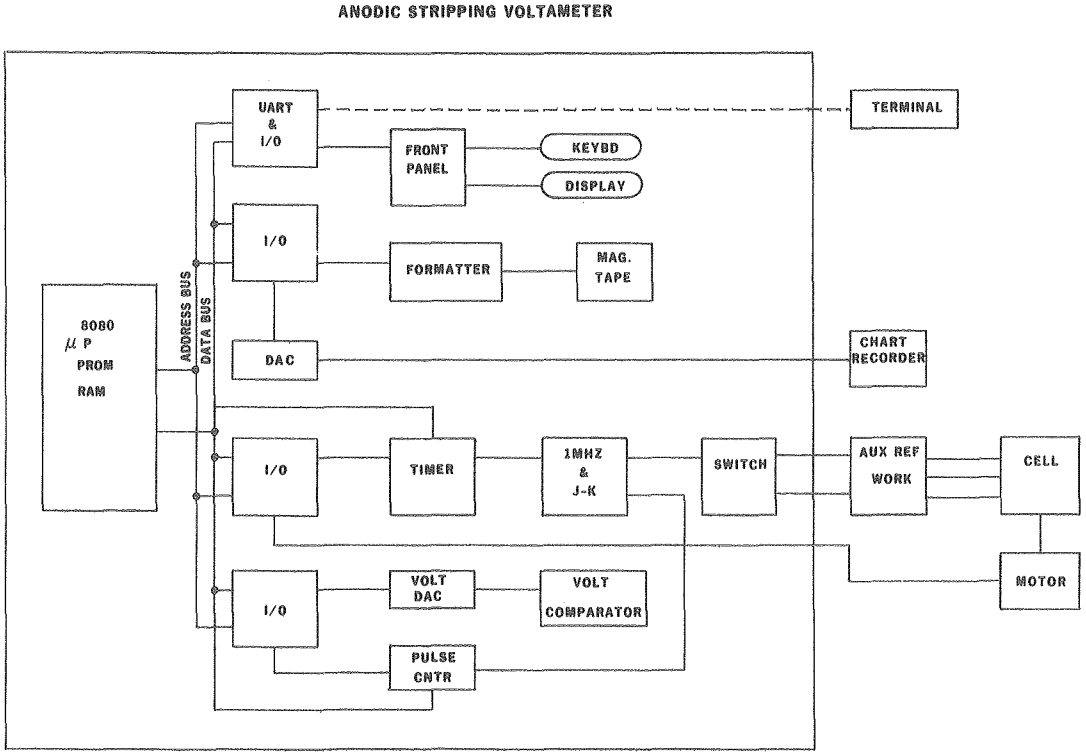

Fig. 1. Block diagram of anodic stripping voltameter. (XBL 794-9252).

Table 1. Major functions of the ASV system components.

Component	Functions
Rotating cell	Contains samples and electrodes, oxygen sparging, preconcentration of trace metals, anodic stripping of amalgams
Digital potentiostat	Applies and maintains plating potential, applies anodic stripping ramp potential, measures stripping peak heights
Microcomputer controller	Start/stop following: cell rotation for sparging, cell rotation for plating, sparge and plating times, anodic stripping ramp, transmits peak height data to cassette and strip chart recorders
Recorder	Strip chart: records background trace, records peak height traces Cassette: Fast rate data storage for later calculation.

gen, e.g., 1-2 L/min., is maintained during the plating step to prevent infusion of oxygen into the cell and thereby maintain a low background current.

Efficient stirring is important for short analysis times such as those used here. Stirring is produced in the rotated cell during plating by controlled periodic reversal of the rotation direction of the cell each second. The graphite working electrode is placed on a radius of the cell and is positioned to face the cell wall. Turning the electrode through 180° until it faces the center of the cell results in a decrease in the rate of amalgam accumulation. This means that the electrode, once positioned and locked into place with the set screw, must not be moved until the analysis is completed.

Digital Potentiostat

The digital potentiostat controls the potential between the working Hg film electrode and the reference electrode by injecting or extracting pulses of charge. The total charge injected is digitized simply by counting the pulses of charge. Advantages of digitization include capability for direct readout on a scaler, and direct computer compatibility.

Microcomputer Controller

In addition to the applied potential, the following functions are also controlled: time for each step, sequencing of each step, storage of the ASV data, output of the data, and a visual indication of the stripping process using a strip chart recorder. Control is provided by a system based on an Intel 8080A 8-bit microprocessor central processing unit. Changes in test parameter variables can be entered by the operator from a 16 button keyboard on the front panel of the instrument. A flow chart detailing the various controlled functions is shown in Figure 2.

The "Power On" or "System Reset" buttons return all parameters to the initial conditions programmed for the plating and stripping parameters. When either of these buttons is pressed, the following preprogrammed values from PROM memories are set into the microprocessor:

Sparge:	60 sec
Start:	1000 mV
Step:	5 mV
Plate:	420 sec
Delay:	1 msec
Count:	400 msec
Day:	0
Test No.:	0
Spike A:	0
Spike B:	0

The MONITOR light will come ON.

Pressing any key will show the value programmed.

To set "SPIKE" press SPIKE and A, or SPIKE and B.

For example, to enter a value for SPIKE B, press SPIKE, press B, press ENTER, press 2, press 5, press ENTER and the change is made. The MONITOR light will go ON. Remember to enter values for Test No. and Day after SYSTEM RESET or Power ON buttons have been pressed.

The software is written in both BASIC and Intel 8080 assembly language. A description of the program is stored on magnetic tapes at LBL and is available on request.

Data Handling

The output signal of analytical interest from the ASV is the stripping peak height as a function of applied potential. For this instrument, the stripping peak heights were measured mainly from the tracing on either a strip chart recorder or an X-Y recorder. Output to the strip chart recorder is the digital-to-analog (DAC) conversion times a scale factor, of the counts accumulated during each 5 millivolt (or other selected step magnitude) step during the stripping cycle. The scale factor (sensitivity) of the strip-chart recording can be chosen by the operator as appropriate for a particular measurement. Data are also recorded on a cartridge digital tape recorder, where they are available for further off-line processing.

Each water analysis is identified by both a test number and run numbers. A complete analysis must have three sequential runs which are performed on: (1) the water sample; (2) the water sample

with spike A added; (3) the same sample with spike B also added. Runs 2 and 3 establish the calibration of the instrument for that analysis. Each run is identified by both test number and run number; a test must have three sequential runs to be valid. If a run is aborted when using the magnetic tape, the test number must be changed before starting a new test. At present, the tape cartridge, which is a 3M DC 300, must be read and analyzed at the LBL Computer Center.

EXAMPLE OF A TAP WATER ANALYSIS

A sample of LBL tap water was obtained by running the water for about 1 - 2 minutes, then collecting 500 mL in a polyethylene bottle which had been cleaned and rinsed with the tap water. Hydrochloric acid was added to pH 1 and the solution permitted to equilibrate for about 48 hours. The sample was then discarded, and an additional 500 mL collected in the same manner. After 48

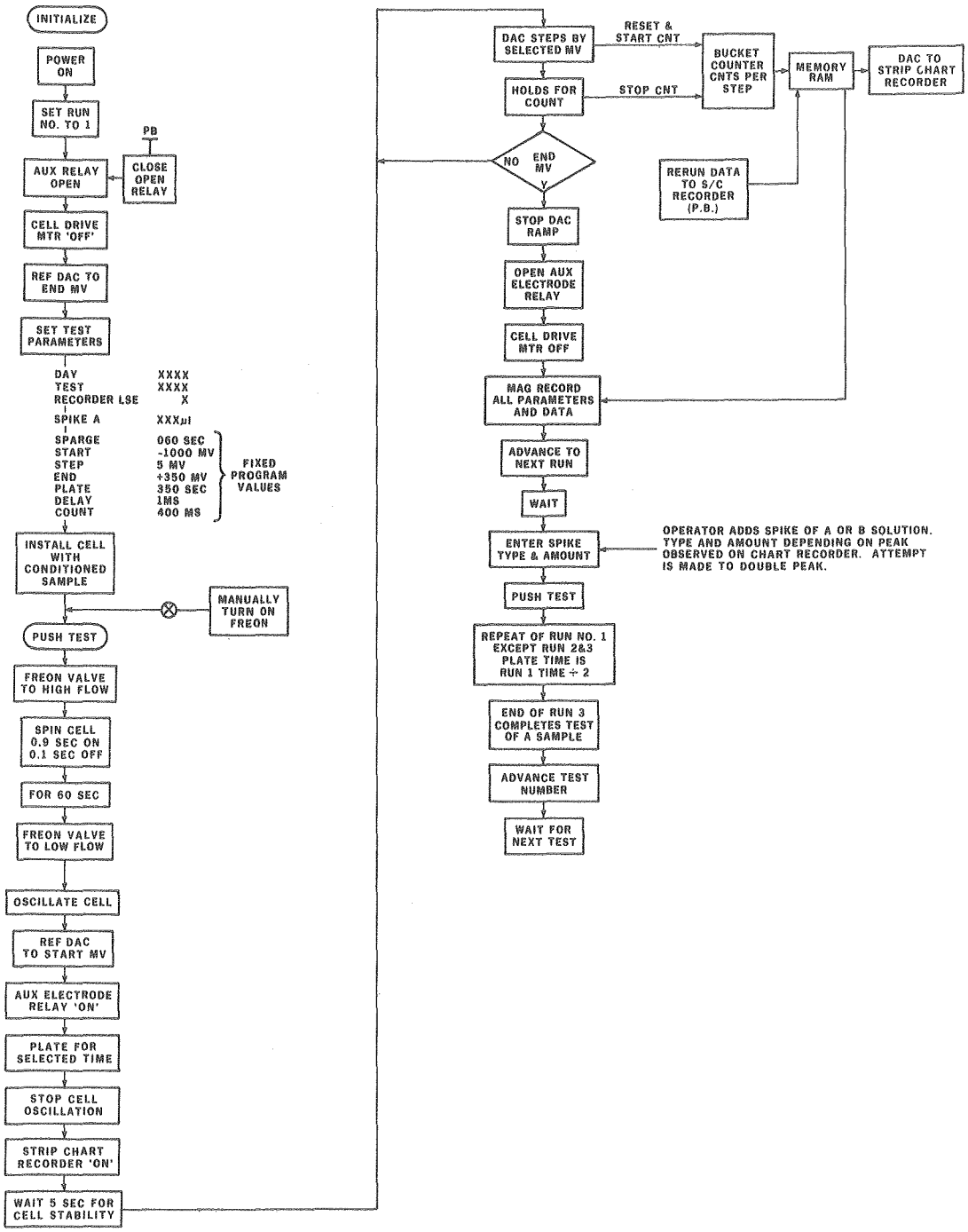

Fig. 2. Flow chart of anodic stripping voltameter. (XBL 794-9471).

hours, 15 mL were added to the rotating cell, and ammonia treated sodium acetate was added to the rotating cell, and ammonia treated sodium acetate was added dropwise to pH 4.7. Then 25 µL of 0.0025 M mercury nitrate solution were pipetted in and background anodic stripping curves obtained. Known µL concentrations of Cd, Cu and Pb standards were pipetted in, and stripping curves again obtained. The peak heights were measured on an X - Y recorder, and the concentrations of the three metals in the tap water were determined by the method of standard additions. Any cadmium in the water was below the limits of detectability of the procedure used, and analysis by atomic absorption did not detect any cadmium. (See Table 2 for LBL and Seattle data.)

PLANNED ACTIVITIES FOR FY 1981

The ASV system is expected to be installed in the EPA mobile laboratory to become part of the water quality monitoring system.

REFERENCES

1. Standard Methods for the Examination of Water and Wastewater, 14th ed., American Public Health Association, Washington, D.C. (1975).

2. J. E. McKee, and H. W. Wolf, Water Quality Criteria, The Resources Agency of California, State Water Resources Control Board, Sacramento, CA (1963).

3. N. I. McClelland and K. H. Mancy, Water Quality Monitoring in Distribution Systems, EPA-600/2-77-074, National Sanitation Foundation, Ann Arbor, MI (1977).

Table 2. Analysis of municipal water samples.

Sample designation	AA values, ppb Cu	AA values, ppb Pb	ASV values, ppb Cu	ASV values, ppb Pb
Seattle, Washington				
NE 24 105NE	1000	10	---	---
7914 NE 26	680	<10	550	1.3
9850 Belfair Rd, Standing	950	<10	1100	N.D.*
9850 Belfair Rd, Running	510	<10	800	N.D.*
Taylor Creek Well 7/4	<6	<10	2.6	N.D.
Taylor Creek Well 7/13	<6	<10	1.4	N.D.
EPA SAMPLES				
Jones Res. Running	---	---	12.4	2.3
Jones Res. Standing	---	---	1800	N.D.*
Park Place Standing, 1st run	---	---	1000	N.D.*
Park Place Standing, 2nd run	---	---	1000	N.D.*
Berkeley, California				
Tap water sample			ASV Values, µg/C Cu 22	Pg 3	Cd <0.2

N.D. = Not detected.

N.D.* = Non-detection likely due to solid phase amalgam formation.

4. S. Miller, Env. Sci. Technol., vol. 14, p. 1287 (1980).

5. F. Vydra, K. Stalek, and E. Julakova, Electrochemical Stripping Analysis, translated by J. Tyson, John Wiley and Sons, Inc., New York (1976).

THE SURVEY OF INSTRUMENTATION FOR ENVIRONMENTAL MONITORING*

M. Quinby-Hunt, C. Case, R. McLaughlin, G. Morton, D. Murphy, A. Nero, and D. Mack

INTRODUCTION

The ever-increasing demand for energy and the demand for a clean environment have made it essential that pollution levels be monitored and regulated. Only through such monitoring can we define existing levels of pollutants and the value of various control strategies. The identification and quantification of pollutants and the evaluation of their impact on ourselves and our environment has resulted in the development of numerous highly sophisticated techniques and instruments. Monitoring methods have been improved by increasing sensitivity, lessening interference, and simplifying data processing, and incorporating automatic operation. However, choosing an analytical method is difficult because of the large variety of instruments and techniques available, the rapid development of new instrumentation, and the large financial investment required.

For the last decade, the Instrumentation for Environmental Monitoring Group of LBL has been investigating and analyzing analytical techniques and instrumentation resulting in a survey, Instrumentation for Environmental Monitoring, which is an aid for individuals responsible for monitoring or controlling pollutants in the environment. Contents include information on current Federal environmental standards and regulations, sources of conventional and radioactive pollutants and their pathways to humans, pollutant forms and characteristics, sampling and calibration techniques, and descriptions of instruments and techniques for monitoring these pollutants. Lawrence Berkeley Laboratory has sold over 4000 volumes to public and private

*This work was supported by the Assistant Secretary for Environment, Office of Health and Environmental Research, Pollutant Characterization and Safety Research Division of the U.S. Department of Energy under Contract No. W-7405-ENG-48.

laboratories, libraries, institutions conducting environmental studies, scientists, engineers administrators, and other groups concerned with protecting the environment. The survey contains four volumes in seven binders: Air (3 binders), Water (2 binders), Radiation (1 binder), and Biomedical (1 binder). Each volume includes several instrument note sections describing the latest commercial instruments.

ACCOMPLISHMENTS DURING FY 1980

During FY 1980 the Survey Group completed two major updates, started work on two other major revisions and a new section, began selection of a publisher to publish existing and new material in book format, started transferring material to a word processing system, and began work on a new direction for the survey.

1. The completed and published update for the Water Volume includes a section describing sources and environmental impacts of halogens and cyanides, analysis methods using ion-selective electrodes, amperometric titrations, and ion chromatography. Another section describes the source and abatement of coliform bacteria and methods of determination. Other sections include information on the significance and determination of solids in various waters and on asbestos in the air and water. This update also includes a multi-paged table describing commercial ion-selective electrodes.

2. The update for the Radiation Volume includes revised sections on these subjects:

- Particle accelerators
- Sources of X-radiation
- Alpha particle instrumentation
- Beta particle instrumentation
- X and gamma monitoring instrumentation
- Gamma spectroscopy

Also included are instrument notes describing commercial monitoring instruments.

3. The Group has almost finished another revision of the Radiation Volume which will include rewritten material on instrumentation for these specific radionuclides:

- Tritium
- Krypton-85
- Radon-222 and its daughters
- Strontium-90 and 89
- Iodine-131 and 129
- Radium
- Uranium
- Plutonium

This update will include instrument notes describing instruments designed to monitor these specific radionuclides.

4. The new Water Volume material will revise the following sections:

- Pesticides
- Phenols
- Petrochemicals
- Oil and Grease

These revisions will include the effect of pollutants associated with new energy conversion technologies and old chemical waste dumps. The impact of the EPA list of priority pollutants will also be discussed. The material will include information on long term effects of oil spills and instrument notes describing GC and LC instrumentation.

5. A new section for the Water Volume will describe sampling techniques in marine, fresh water, and wastewater environments. Information will include sampling methodologies; logistics such as sampling frequency, site selection, and sampling profile; sources of sample contamination and contamination prevention; sample storage and pretreatment; and sampling techniques for specific energy related pollutants. The section will also include instrument notes.

6. For the last decade, LBL has distributed the survey in loose-leaf binders. We are now selecting a publisher to produce the survey in a more standard textbook format. This publisher will handle advertising, process orders, and maintain an inventory. The effect should be to expand circulation by offering the volumes at lower cost. We plan to revise certain volumes every few years. Instrument notes will probably be published separately.

7. We are investigating a new direction for the survey which will more closely relate the material to certain energy producing technologies such as oil-shale and coal conversion, and to energy related pollutants such as acid-rain. Material in current updates and new sections will reflect this new direction. The survey group is also considering a fifth volume concerning monitoring of energy related pollutants.

8. Finally, the survey group is transferring most of the present material to a text processing system. This will facilitate updating the material, writing new sections, and making changes suggested by reviewers. A phototypesetter will print the material.

PLANNED ACTIVITIES FOR FY 1981

The planned activities for FY 1981 include finishing the Radiation and Water volume updates, selecting a publisher, publishing the Radiation Volume as a book, and preparing the Water Volume for book publication. In addition, the group plans to start a major update on the Air Particulates Section of the Air Volume and to prepare a new section on biomass indicators for the Water Volume. Work will continue on the new direction for the survey and the presentation of material on energy related pollutants.

THE POSSIBLE CHRONDRITIC NATURE OF THE DANISH CRETACEOUS-TERTIARY BOUNDARY*

F. Asaro, H. Michel, L. Alvarez, and W. Alvarez

INTRODUCTION

Our research to date has demonstrated that deep-sea limestones exposed in Italy,[1-3] Denmark,[4] New Zealand,[4] and northern Spain[5] show unusual increases in the abundance of iridium (Ir) above the background level at exactly the time of the Cretaceous-Tertiary (C-T) extinctions, 65 million years ago. As Ir is much depleted on the earth's surface with respect to the average solar system abundance, such an enrichment is not likely to have come from a terrestrial source because extraterrestrial sources contain 3 orders of magnitude more Ir than terrestrial sources and are much more likely to have produced the enrichment. Measurement of the isotopic ratio of the two iridium isotopes in the Italian C-T boundary layer showed that it was identical with that of a terrestrial source.[1] This eliminated a supernova explosion 65 million years ago as a source of the iridium. An interstellar origin for the asteroid, as postulated by Napier and Clube for impacting planetesimals,[6] would only be possible if isotopic ratios (at least for Ir) in our part of the galaxy were nearly constant. Many sources of extraterrestrial material from within the solar system were considered and subjected to three tests. These sources had to be (1) able to deposit the Ir, (2) able to cause the C-T extinctions, and (3) likely to have occurred about 65 million years ago. Only one source survived the tests.

ASTEROID-IMPACT HYPOTHESIS

We have developed an asteroid-impact theory that satisfied these conditions and many others.[1] The theory assumes the following events. An Apollo object, with about a 10 km diameter, struck the earth 65 million years ago. It vaporized as did a much larger mass of terrestrial material. About 20 percent of this combined mass, modeled after the volcanic explosion of Krakatoa, ended up in the stratosphere, encircled the earth, and blocked out nearly all of the direct sunlight. Photosynthesis then stopped. The larger animals, which depended on the plant food chain, died while some smaller animals, needing less food, survived. Some seeds could have survived for several years and then reestablished the plants after the dust cloud sank to earth and direct sunlight reappeared. Mass extinctions of this type have occurred about every 100 million years.

*Later stages of this work were partially supported by the California Space Group and the National Aeronautics and Space Administration Ames Research Center and by the U.S. Department of Energy under Contract No. W-7405-ENG-48.

SUMMARY OF RESEARCH BY OTHER INVESTIGATORS

Dutch geologists, after learning of the Italian Ir data, found a similar Ir anomaly in a rock section from Caravaca (Barranco-del-Gredero) in southeast Spain.[7] We were able to confirm the iridium abundances in a sample supplied by J. Smit and to determine the variation in abundance within a few centimeters of the C-T boundary.[8] Smit and Hertogen[7] also measured the abundances of another platinum group element, osmium, which also exhibited an anomalously high abundance at the C-T boundary near Caravaca. These authors also stated the ratio of two osmium isotopes in the C-T boundary was indistinguishable within 0.1 percent from the terrestrial (i.e., solar system) ratio.

Concern has been expressed[9,10] about the correctness of the stratigraphy upon which the selection[1] of our Italian samples was based. However, very recent work[11] on a deep-sea core from the southeastern Atlantic Ocean near South Africa, supported the Italian stratigraphy.

There have been a number of suggestions in the past that an extraterrestrial object impacting on the earth caused or could cause massive extinctions of life. E. J. Öpik,[12] for example, discussed the lethal effects which could be caused by the heat generated from such objects striking the earth, and H. C. Urey[13] stated specifically that a comet was probably the cause of Cretaceous-Tertiary extinctions.

Events likely to occur if sunlight were temporarily "turned off" have also been discussed.[14] Our deduction, in contrast to others, is based on physical science data (the iridium anomaly) and is the only explanation we found which explained the Ir anomaly, could cause the massive extinction of life and was likely to occur in a period of ∿100 million years.

Smit and Hertogen[7] also concluded a large meteorite may have struck the earth and caused the extinctions. K. J. Hsü[15] suggested the extinctions were caused by cyanide poisoning resulting from a cometary impact; and Cesare Emiliani[16] proposed that a sudden heat flash, possibly caused by an asteroid impact, could have caused the C-T extinctions. Ganapathy[17] measured the abundances of Pt group elements (Ru, Pd, Re, Os, Ir, Pt), Au, Co and Ni in the Danish C-T boundary layer and confirmed that it contained a chondritic component. Kyte et al.[18] measured Pt group elements in the Danish boundary layer. They also found Ir in a deep sea core from the Central Pacific (hole 465a) (we have also extensively studied samples from this hole). Kyte et al. believe that an extraterrestrial projectile consisting of a metal sulfide core, interstellar

matter, or structurally weak cometary matter was the source of the platinum group elements. They do not think a chondritic asteroid or a comet could be the source.

REVIEW OF 1980 STUDIES AND RESEARCH

We have observed the Ir anomaly in uplifted marine sediments in five locations in Italy, one in Denmark, three in Spain (besides that found by Smit and Hertogen), and one in New Zealand. Ir has been found in one (hole 465a) of two deep-sea cores. The validity of the asteroid-impact theory would be in doubt if the Ir anomaly is not found wherever the C-T boundary is intact. The deep sea core in which the Ir anomaly was not found (hole 356) was in the South Atlantic; it will be studied further.

Measurements of the abundances of platinum group elements have been made in a C-T boundary layer sample from Denmark. Figure 1 shows the ratio of abundances of different elements to that of Ir in various mantle materials, divided by the same quantities for Cl chondrites.[19] The Pt and Au ratios approach the chondritic abundances as the degree of partial melting of the mantle gets higher. An ultra-basic nodule,[20] which may represent the mantle, has very close to the chondritic ratios for Ir and Pt. Some of our recent measurements of Pt, Au, and non-volatile Os, as well as Ir, in the Danish C-T boundary layer are shown in Figure 1 and Table I. The Pt and Ir data are

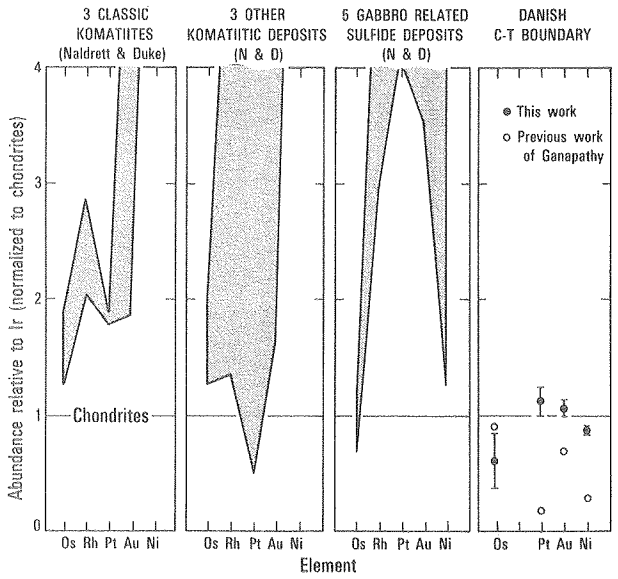

Fig. 1. Relative abundances of some platinum group elements, gold, and nickel with respect to iridium. Each abundance was divided by the abundance of that element, except for Rh, in Type I carbonaceous chondrites. Rh abundances were divided by Rh abundances in other types of chondrites because Cl values were not available. Errors in the LBL measurements reflect one sigma value of the counting errors, except for the Au error which is the root mean square deviation of 6 measurements, as the 6 values were not consistent within counting errors. The Os measurement was on a nitric-acid-insoluble residue which had been fired to 800°C. (XBL 809-1964)

Table 1. Possible chondritic nature of the Danish C-T boundary.[a]

	Ganapathy[b] (Average of 2)	Our Work[c]	Cl Chondrites[d]
Pt/Ir	0.40	2.24 ± 0.23	1.98
Ni/1000 Ir	6.2	16.6 ± 0.5	20
Co/1000 Ir	0.82	2.07 ± 0.03	1.01[e]
Au/Ir	0.21	0.319 ± 0.020	0.296

[a]If the C-T boundary includes an asteroid component with chondritic abundancies, the ratios of the abundances of various elements to Ir should be larger than chondritic because of terrestrial contributions.

[b]Ratios were calculated from abundances given in Ganapathy.[17]

[c]Pt and Au data are from unpublished work of F. Asaro, H.V. Michel, W. Alvarez, and L.W. Alvarez, 1980. Other data are from Ref. 1.

[d]Au and Ir data are from U. Krähenbühl et al.[24] Pt datum is from Ehmann and Gillum.[25]

[e]The Co abundance is a weighted average (507 ppm) of the data given by Moore.[26]

consistent with a chondritic origin, as predicted by the asteroid-impact theory. Part of the data of Ganapathy is also included in Figure 1 and Table I. In addition to measurements of Pt group elements on the Danish and other C-T boundary layers, similar measurements are needed on nearby Cretaceous and Tertiary rock formations. $^{187}Os/^{186}Os$ isotopic ratios[21] might determine if the Os and Re have maintained chondritic relative abundances throughout the predominant part of their existence since coalescence from dispersed materials billions of years ago.

More studies of the clay mineralogy of the C-T boundary layer are needed. These may indicate if the boundary deposition was associated with an extraordinary event.

Rare earth abundances patterns, particularly of the clay fraction, may also help determine the origin of the terrestrial components. Rare earth patterns in clay fractions of sediments tend to inherit the patterns of the rocks from which they originated.[22] Figure 2 shows several examples of the rare earth abundance patterns of nitric-acid-insoluble residues from the Danish boundary layer and the limestones above and below. Such patterns along with the other chemical data may indicate the type of rock from which the boundary layer originated. This may help indicate if the origin was continental, sea floor, rift, or otherwise.

The intensity of the C-T iridium anomaly as a function of geographical location along with the mineralogical and chemical studies of the boundary layers may suggest an impact location when considerably more data are obtained. If the asteroid-impact theory is correct, the extinctions should be repetitive and the Ir anomaly should be observed in other geological stratigraphic levels corresponding to known extinctions. About five other massive extinctions, in addition to the event at the end of the Cretaceous Period, have been noted.[23] These come at the end of the Cambrian (∿500 MY ago), the Ordovician (∿435 MY ago), the Devonian (∿345 MY ago), the Permian

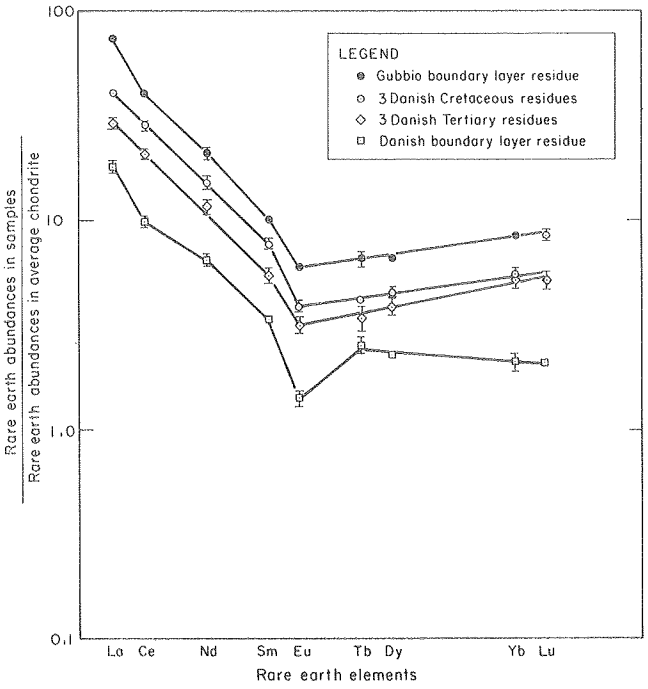

Fig. 2. Rare earth abundance patterns as normalized to the data of Masuda et al. except for Tb, for the Leedy L6 meteorite.[27] The Tb abundance in meteorites is assumed to be 0.059 ppm. Errors for the Danish Cretaceous (3 samples) and Tertiary (2 samples) nitric-acid-insoluble residues are root-mean-square deviations. Errors for the nitric-acid-insoluble residues from the Gubbio and Danish boundary layers are 1 sigma values of the counting errors. (XBL 7911-13249)

(∿230 MY ago) and the Triassic (∿195 MY ago) Periods.

PLANNED FUTURE ACTIVITIES

In the next four years, we plan to: test the concept of world-wide distribution of the Ir anomaly and the premise of an extraordinary extraterrestrial origin of the anomaly; attempt to determine the location of the C-T impact site, and test the repetitive nature of the proposed impact. From the results of these tests and the questions which will develop, the extent to which the theory is correct can be evaluated and the need and direction for future work can be assessed.

REFERENCES

1. L. W. Alvarez, W. Alvarez, H. V. Michel and F. Asaro, "Extraterrestrial Cause for the Cretaceous-Tertiary Extinction," Science, vol. 208, pp. 1095-1108 (1980).

2. W. Alvarez, L. W. Alvarez, F. Asaro and H. V. Michel, "Experimental Evidence in Support of an Extraterrestrial Trigger for the Cretaceous-Tertiary Extinctions," EOS Trans. Am. Geophys. Union, vol. 60, p. 734 (1979).

3. W. Alvarez, L. W. Alvarez, F. Asaro and H. V. Michel, "Anomalous Iridium Levels at the Cretaceous-Tertiary Boundary at Gubbio, Italy: Negative Results of Tests for a Supernova Origin," Geol. Soc. America Abstract, vol. 11, p. 378 (1979).

4. D. Russell, L. W. Alvarez, W. Alvarez, H. V. Michel and F. Asaro, unpublished data (1980) cited in Ref. 1.

5. M. Arthur, L. W. Alvarez, W. Alvarez, H.V. Michel and F. Asaro, unpublished data, 1980.

6. W. M. Napier and S. V. M. Clube, "A Theory of Terrestrial Catastrophism," Nature (London), vol. 282, pp. 455-459 (1979).

7. J. Smit and J. Hertogen, "An Extraterrestrial Event at the Cretaceous-Tertiary Boundary," Nature, vol. 285, pp. 198-200 (1980).

8. L. W. Alvarez, W. Alvarez, H. V. Michel and F. Asaro, unpublished data, 1979. Ir values are plotted in Ref. 7.

9. F. C. Wezel, "The Scaglia Rossa Formation of Central Italy: Results and Problems Emerging from a Regional Study," Ateneo Parmense, Acta Nat., vol. 15, pp. 243-259 (1979).

10. Finn Surlyk, "The Cretaceous-Tertiary Boundary Event," Nature, vol. 285, pp. 187-188 (1980).

11. K. S. Hsü, private communication to Walter Alvarez and News Release NSF PR 80-56 (1980).

12. E. S. Öpik, "On the Catastrophic Effects of Collisions with Celestial Bodies," Irish Astronomical Journal, vol. 5 no. 1, p. 34 (1978).

13. H. C. Urey, "Cometary Collisions and Geological Periods," Nature, vol. 242, p.32 (1973).

14. K-TEC group (P. Beland et al.). "Cretaceous-Tertiary Extinctions and Possible Terrestrial and Extraterrestrial Causes," Proceedings of Workshop, National Museum of Natural Sciences, Ottawa, 16 and 17 November 1976, pp. 144-149 (1976).

15. K. J. Hsü, "Terrestrial Catastrophe Caused by Cometary Impact at the End of the Cretaceous," Nature, vol. 285, pp. 201-203 (1980).

16. Cesare Emiliani, "Death and Renovation at the End of the Mesozoic" EOS, vol. 61, no. 26, pp. 505-506 (1980).

17. R. Ganapathy, "A Major Meteorite Impact on the Earth 65 Million Years Ago. Evidence from the Cretaceous-Tertiary Boundary Clay," Science, vol. 209, pp. 921-923 (1980).

18. F. T. Kyte, Z. Zhou and J. Wasson, Submitted to Nature (Oct. 1980).

19. Data for basic materials was taken from "Platinum Metals in Magnatic Sulfide Ores" by A. J. Naldrett and J. M. Duke, Science, vol. 208, pp. 1417-1424, (1980).

20. L. P. Greenland, D. Gottfried, and R. I. Tilling, "Iridium in Some Calcic and Calc-Alkaline Batholithic Rocks of the Western United States," Chem. Geol., vol. 14, pp. 117-122 (1974); reported in J. H. Crocket, "Platinum-Group Elements and Mafic and Ultramafic Rocks: A Survey," Canadian Mineralogist, vol. 17, pp. 391-402 (1979).

21. C. J. Allègre and J. M. Luck, "Osmium Isotopes as Petrogenetic and Geological Tracers," Earth Planet. Sci. Lett. vol, 48, pp. 148-154 (1980).

22. R. L. Cullers, Long-Tsu Yeh, S. Chaudhuri, and C. V. Guidotti, "Rare Earth Elements in Silurian Peltic Schists from N. W. Maine," Geochim. Cosmochim. Acta, vol. 38, pp. 389-400, (1974).

23. N. D. Newell, "Crises in the History of Life," Scientific American, vol. 208, no. 2, pp. 76-92 (1963).

24. U. Krähenbühl, S. W. Morgan, R. Ganapathy and E. Anders, "Abundance of 17 Trace Elements in Carbonaceous Chondrites," Geochem. Cosmochim. Acta, vol. 37, pp. 1353-1370 (1973).

25. W. D. Ehmann and D. E. Gillum, "Platinum and Gold in Chondritic Meteorites," Chem. Geol., vol. 9, pp. 1-11 (1972).

26. B. Mason, (ed.), Handbook of Elemental Abundances in Meteorites, Gordon and Breach Science Publishers, London (1971).

27. A. Masuda, N. Nakamura and T. Tanaka, "Fine Structures of Mutually Normalized Rare-Earth Patterns of Chondrites," Geochim. Cosmochim. Acta, vol. 37, pp. 239-248 (1973).

IMPROVEMENT OF THE SENSITIVITY AND PRECISION OF NEUTRON ACTIVATION ANALYSIS OF SOME ELEMENTS IN PLANKTON AND PLANKTONIC FISH*

F. Asaro, H. Michel, R. Flegal,† and Quinby-Hunt

The normal LBL method for measuring elemental abundances using neutron activation analysis was designed to maximize the precision for measurements on substances with approximately the composition of the average earth's crust. The standard procedure needs to be modified for materials with an abundance of many trace elements much lower than normally present in the earth's crust and with an abundance of Na of approximately 10 percent.

The sample preparation procedure was modified by pressing the pellets in a die made of Al_2O_3 instead of tool steel.

The neutron irradiation for measuring the short lived elements Al, Cl, Mn, Mg, Cu, Ca, K, Na, Ga, Dy, Ba, and In was reduced from 18 minutes at 11 kw to 3 minutes at 11 kw. The gamma-ray spectrum of each irradiated unknown was counted for 1 minute, approximately 9 minutes after bombardment began (a normal gamma-ray counting procedure). The samples were counted again for 12 minutes each about one hour after irradiation (instead of the normal 6 minutes) and recounted the following day for 2 hours. Table 1 shows the sensitivities and precision obtained with these procedures.

Table 1. Element sensitivities obtained after a 3 min. neutron irradiation (2.7 n/sec-cm^2) in plankton samples containing large amounts of Na and Sr.

Element	Sensitivity (or precision) for a 95% confidence limit
Al[a,b]	0.3%
Ba[c,d]	176 ppm
Ca[a]	2.8%
Cl[a]	32%
Cu[e]	86 ppm
Dy[c]	0.9 ppm
Ga[e]	142 ppm
In[c]	0.7 ppm
K[e]	0.7%
Mg[a]	4.6%
Mn[c]	8 ppm
Na[e]	.09% precision when abundance is 10.3%
Sr[c,d]	.15% precision when abundance is 3.1%
Ti[a,d]	.21%

[a]Data is from the 1.00 min. counts taken ∿9 minutes after the irradiation.

[b]The Al radiation can also result from irradiated Si (from SiO_2). 100% SiO_2 appears as 0.51% Al.

[c]Data is from the 12.00 min. counts taken ∿1 hour after the irradiation.

[d]Better data can be obtained following a long irradiation.

[e]Data is from the 120.00 min. counts taken ∿1 day after the irradiation.

* This work was supported by the Assistant Secretary for Conservation and Solar Energy, Office of Solar Power Application, Ocean Energy Systems Division of the U.S. Department of Energy under contract W-7405-ENG-48.

†Moss Landing Marine Laboratory

A significant improvement in the sensitivity of detection of the longer lived isotopes is gained by using a large 128 cc Ge-Li detector, instead of a 7 cc Ge detector, and counting for longer periods of time.

Table 2 compares the elemental abundance determined normally with the estimated abundance determined with the large Ge-Li detector. Sample P7 is plankton and FD is planktonic fish. In addition to elements already discussed, 16 were measured and 13 were detected in plankton samples.

In the case of marine base-line studies on plankton and fish, where precision and detection of trace elements is critical to the assessment of environmental impact, this improvement in measurement capability is important. The samples were supplied by Dr. Russ Flegal of the Moss Landing Marine Laboratory and Dr. George Knauer of the California Institute of Technology.

Table 2. Estimates[a] of abundances in plankton determined with a 128 cc Ge-Li detector, ppm.

Sample	γ ray detector volume	Elements						
		Co[6]	Cr	Cs	Fe	Hf	Ir	Ni
P7	128cc[c]	.446±.006	1.06±.17	.0066±.008	29.2±1.5	<.010	<.00028	5.84±.11
	7cc[d]	.472±.026	<1.9	.032 ±.018	<84	<.07	<.0018	6.4 ±1.0
FD	128cc[e]	.127±.007	.17±.04	.0503±.0011	34.6±.9	<.0032	<.00009	1.60±.07
	7cc[d]	.111±.018	<1.2	.056 ±.016	<74	<.07	<.0035	<3.2

Sample	γ ray detector volume	Elements					
		Rb(+Sr)[f]	Sb[g]	Ta[g]	Th	Ag	Sr
P7	128cc[c]	3.30±.21	.173 ±.004	.0055±.0005	<.021	.04±.004	-
	7cc[d]	2.0 ±.6	.138 ±.026	<.020	<.08	<.16	-
FD	128cc[e]	6.97±.18	.0154±.0012	.00135±.00018	<.008		576±14
	7cc[c]	7.5 ±.7	<.029	<.024	<.05		460±110

[a]Only estimates were obtained for the measurements made with the 128 cc detecter because flux monitors were used for all elements. Uncertainties of ∿10% are possible due to calibration. The listed errors are 1σ values of the counting error and would be the precision if a multi-element standard were used.

[b]Abundances have been modified to reflect an estimated .03-.04 ppm Co contribution from the Al wrapping foil.

[c]464 minute gamma-ray count about 70 days after the end of the long irradiation.

[d]60 minute gamma-ray count about 24 days after the end of the long irradiation.

[e]754 minute gamma-ray count about 71 days after the end of the long irradiation.

[f]The ^{86}Rb radiation is also produced by the reaction ^{86}Sr (n,p) ^{86}Rb. The Sr contribution has not been removed. Sea water and Sr probably account for all the ^{86}Rb detected in P7 and very little of that detected in FD.

[g]Estimated contaminants from the Al wrapping foil of ∿.001→.004 ppm for Ta and ∿.01 ppm for Sb have not been removed. Accurate abundances of these elements can be obtained by removing the Al foil from each of the pills and measuring its gamma-ray spectrum.

SOURCES OF SOME SECONDARILY WORKED OBSIDIAN ARTIFACTS FROM TIKAL, GUATEMALA*

H. Moholy-Nagy, F. Asaro, and F. Stross

A small series of secondarily-worked obsidian artifacts from Tikal, Guatemala, was analyzed to determine the source of the stone. The results of this analysis shed light upon obsidian procurement at Tikal and also relate to obsidian source studies in general.

Tikal seems to have imported obsidian throughout its history. Although most obsidian found at Tikal is grey or black in color, a small proportion, estimated at about 2 percent of the recorded total, is green. Green obsidian is consistently present after the beginning of the Classic Period, with the highest frequency occurring during the Early Classic. Source analyses carried out on Mesoamerican obsidian since the late 1960s[1] strongly suggest that all green obsidian found in the Maya area comes from quarries in the vicinity of Pachuca, Hidalgo, Central Mexico.

Source analysis by X-ray flourescence (XRF) or neutron activation analysis (NAA)[2] provides a possibility for confirming or dicarding hypotheses about sources suggested by other data, such as differences in artifact forms, color of the obsidian, manufacturing techniques, or archaeological context.

Samples taken from 28 incomplete artifacts were analyzed: 14 point-knives, 4 obsidian eccentrics, 2 incised obsidians, a ground obsidian earspool, 3 prismatic blades, and 2 cortical flakes from Tikal, and 2 flakes from Tetitla, Teotihuacan, Mexico. The secondarily worked point-knives, eccentrics, and incised obsidians were the main focus of the analysis. The ground earspool of grey obsidian was analyzed because of its uniqueness at Tikal. At the time of its discovery, it was felt that the earspool represented additional evidence of influence from Central Mexico. The prismatic blades, two grey and one brown-green, were chosen because of their unusual optical properties. The two small grey cortical flakes seem to be debitage and might therefore support the hypothesis that Highland obsidian arrived in Tikal as core preforms. The two waste flakes from Tetitla, Mexico, were analyzed for comparison with the Tikal materials.

The source of the obsidian was first determined by XRF (Table 1) and then confirmed by an abbreviated NAA on a representative sample from each provenience group (Table 2). Any artifacts still unassigned by the abbreviated NAA were submitted to a more intensive NAA measurement that might involve twenty to thirty elements (Table 3). This procedure was successful in assigning the obsidian used for all artifacts except two point-knives (TIKL-10 and TIKL-11). The detailed analysis of these two opaque black specimens is given in Table 3. The stone used for one specimen, TIKL-11, is similar to obsidian from Zinapecuaro, Michoacan, Mexico.

No transparent or translucent green obsidian point-knives were selected for analysis because it was assumed that the source of the stone was Pachuca, Hidalgo. However, one fragment of an unusual, opaque, silver-green obsidian point-knife was analyzed (45G-11/7, TIKL-6), and this also proved to be from the Pachuca area. Of the 13 other grey and black point-knives, nine were made of Mexican obsidian, seven of these of stone from Otumba. Two point-knives were made of obsidian from the Guatemalan highlands source of Ixtepeque. Two, as noted above, could not be attributed to a source.

Although the size of the sample is small, the results of the analysis generally support the hypothesis that obsidian eccentrics and incised obsidians were locally manufactured from core preforms from the Guatemalan Highlands. The circumstance that these ceremonial artifacts were made of El Chayal obsidian reinforces the relationship between ceremonial use of obsidian at Tikal and the predominantly utilitarian prismatic blade manufacture already suggested by a behavioral typology and previous, less accurate source analyses.

Analysis results also indicate that most of the grey obsidian point-knives found at Tikal are Central Mexican products, not local imitations of Central Mexican types. This finding supports the observations of specialized obsidian workshops in the Basin of Mexico.

Present evidence examined at Mesoamerican quarries indicates that raw obsidian was rarely, if ever, transported any distance. Usually, some preliminary working into core preforms or macroblades took place in workshops near the quarries.[7-10]

The analysis of this sample of secondarily-worked artifacts has confirmed earlier suggestions that Tikal imported most of its obsidian from the Guatemalan highlands, predominantly as core preforms. During the Classic Period, Tikal also received a very small amount of obsidian from Central Mexico, predominantly as finished point-knives and green obsidian prismatic blades. The inception, as well as the high point, of this latter obsidian exchange network coincides with the time of maximum Teotihuacan influence in other aspects of Tikal material culture during the Early Classic period.

Although the presence at Tikal of Central

*This work was supported by Tikal Project, University Museum, University of Pennsylvania, Philadelphia, PA and by the U.S. Department of Energy under Contract No. W-7405-ENG-48.

Table 1. Results of x-ray fluorescence analysis (XRF).

Sample (Number of artifacts)	Ba[a] (ppm)	Ce (ppm)	Rb/Zr	Sr/Zr
Artifacts assigned to El Chayal-La Joya-Cornelia Dome (Guatemala) source				
Mean (8)	897	51.6	1.23	1.33
RMSD[b](8)	21	4.2	0.07	0.04
TIKL-15	896	48 ± 6	0.99	1.25
Reference Group:				
Asaro et al. (1978)	943	47.4	1.24	1.29
Artifacts assigned to Ixtepeque (Jutiapa) source (R. Sidrys' 2-1 source)				
Mean (3)	1010	46	0.56	0.88
RMSD[b](3)	17	4.4	0.03	0.04
Reference Group:				
Asaro et al. (1978)	1030	43.3	0.57	0.90
Artifact assigned to San Martin Jiloteqeque area (Chimaltenango) (Rio Pixcaya type)				
TIKL-22	1051	47 ± 4	0.85 ± 0.05	1.66 ± 0.06
Reference Group:				
Asaro et al. (1978)	1103	47.4	0.95	1.64
Artifact assigned to Ucareo (Michoacán) type				
TIKL-4	159	74 ± 6	1.18 ± 0.07	0.08 ± 0.02
Reference Group:				
Asaro et al. (1975)	138 ± 19	71 ± 2	1.24	0.11
Artifacts assigned to Otumba (Mexico) source				
Mean (9)	751	59	0.83	0.87
RMSD[b](9)	29	6	0.07	0.05
Reference Groups:				
Stross et al. (1976)	880-1000	60-65	∿1.0	∿1.0
Asaro et al. (1975)	806 ± 26	54.9 ± 0.8		
Artifacts assigned to Pachuca (Hidalgo) source				
Mean (2)	16	102	0.21	<0.008
RMSD[b](2)	10	6	0.01	
Reference Groups:				
Stross et al. (1976)	0-10	110-115	0.25	<0.006
Asaro et al. (1975)		96.4 ± 1.9		
Artifact assigned to Zaragoza (Puebla) source				
TIKL-3	434	82 ± 13	0.67	0.15
Reference Group:				
Stross et al. (1976)	500	70	0.79	0.21
Asaro et al. (1975)	474 ± 21	75.9 ± 9		

[a]Uncertainty in the Ba measurement (except for Pachuca results) is about 4%.

[b]RMSD is the root-mean-square-deviation.

Mexican green obsidian has been known for a number of years, the presence of Mexican grey obsidian was discovered by analyzing point-knives. Therefore, in attempting to trace obsidian procurement networks for any particular site or region,[11] samples should be taken from as many different types of artifacts present as possible. In assessing the qualities of materials, ancient craftsmen made fine distinctions between materials that are now lost to us or that we are just beginning to appreciate.

In this type of study it is of particular interest that recent developments in method permit increased precision in the sourcing of obsidian by XRF and NAA.

Acknowledgments: The authors thank William R. Coe for his generous support, and Payson D. Sheets for his helpful criticism.

REFERENCES

1. F. H. Stross, J. R. Weaver, G. E. A. Wyld, R. F. Heizer, and J. A. Graham, "Analysis of American Obsidian by X-ray Fluorescence and Neutron Activation Analysis," in Contributions of the University of California Archaeological Research Facility, No. 4, pp. 59-79, Berkeley, California (1968).

2. F. Asaro, H. V. Michel, R. Sidrys, and F. Stross, "High-Precision Chemical Characterization of Major Obsidian Sources in Guatemala," American Antiquity, vol. 43, pp. 436-443 (1978).

3. F. H. Stross, T. R. Hester, R. F. Heizer, and R. N. Jack, "Chemical and Archaeological Studies of Meso-American Obsidians," in Advances in Obsidian Glass Studies: Archaeological and Geochemical Perspectives,

Table 2. Neutron activation verification of XRF assignments.

Artifact	Element abundances[a] and errors[b] Mn	Ba	Dy	Na %	K %
TIKL-4	164±2	154±18	3.93±0.08	2.86±0.03	4.43±0.30
Ucareo Reference Group	170±4	162±12	3.82±0.10	2.91±0.03	4.27±0.25
TIKL-12	453±5	1064±28	2.49±0.10	3.08±0.03	4.21±0.32
Ixtepeque Source (Sidrys' 2-1 source)	449±9	1030	2.30±0.11	3.05±0.06	3.61±0.26
TIKL-21	640±6	922±35	2.73±0.12	3.25±0.06	3.83±0.27
TIKL-15	639±6	926±32	2.60±0.11	3.21±0.03	3.58±0.31
El Chayal - La Joya-Cornelia Dome Source	649±13	943	2.66±0.11	3.15±0.06	3.45
TIKL-22	529±5	1130±34	2.18±0.11	2.96±0.03	3.59±0.30
San Martin Jilotepeque Area (Rio Pixcaya Type)	521±10	1036±40	2.10±0.11	2.92±0.06	3.71±0.24
TIKL-24	1132±11	<130	16.63±0.21	3.96±0.04	3.75±.37
Pachuca Type	1132±25	<36	16.46±0.34	3.81±0.13	3.64±0.46
TIKL-1	389±4	811±28	3.54±.10	3.24±.06	3.57±.25
TIKL-5	395±4	758±25	3.61±.10	3.16±.03	3.83±.30
LBL-391 (ppm) Mn Type (very likely Otumba, Mexico source)	391±6	839±21	3.29±0.14	3.15±0.06	3.64±0.46
TIKL-3	250±5	432±25	5.11±0.10	3.13±0.06	4.17±0.24
LBL-252(ppm)Mn type (very likely Zaragoza, Puebla source)	252±5	488±14	4.93±0.10	3.05±0.06	4.16±0.12

[a]Abundances are given in percent for Na and K and in parts-per-million (ppm) for the other elements.

[b]The errors for the individual artifacts reflect the precision of the measurement. For the reference groups, the error is the standard deviation or root-mean-square-deviation (RMSD).

R. E. Taylor, ed., Noyes Press, Park Ridge, New Jersey, pp. 240-258 (1976).

4. F. Asaro, F. H. Stross, and H. V. Michel, Unpublished data (1975).

5. J. E. Ericson and J. Kimberlin, "Obsidian Sources, Chemical Characterization and Hydration Rates in West Mexico," Archaeometry, vol. 19, no. 2, pp. 157-166 (1977).

6. I. Perlman and F. Asaro, "Pottery Analysis by Neutron Activation," in Science and Archaeology, R. H. Brill, ed., Massachusetts Institute of Technology Press, Cambridge, Massachusetts and London, England, pp. 182-195 (1971).

7. W. H. Holmes, Handbook of Aboriginal American Antiquities, Part 1. Introduction: The Lithic Industries, Bureau of American Ethnology, Bulletin 60, Washington, D. C. (1919). Burt Franklin Reprints, New York (1974).

8. M. W. Spence and J. R. Parson, "Prehistoric Obsidian Mines in Southern Hidalgo," American Antiquity, vol. 32, no. 4, pp. 542-543 (1967).

9. J. A. Graham and R. F. Heizer, "Notes on the Papalhuapa Site, Guatemala," in Contributions of the University of California Archaeological Research Facility, No. 5, pp. 101-125, Berkeley, California (1968).

10. P. D. Sheets, "Behavioral Analysis and the Structure of a Prehistoric Industry," Current Anthropology, vol. 16, no. 3, pp. 369-391 (1975).

11. N. Hammond, "Obsidian Trade Routes in the Mayan Area," Science, vol. 178, p. 1092 (1972).

Table 3. Detailed analysis of two unassigned artifacts. (NAA except where indicated.)

	68I-45/20 (TIKL-10)	77A-17/7 (TIKL-11)	Zinapecuaro (LBL)	Zinapecuaro (Ericson & Kimberlin)
Al%	7.28 ± 0.13[a]	6.51 ± 0.10[a]	6.59 ± 0.15[b]	
Ba	773 ± 18	34 ± 9	74 ± 12	[c]
Ce	60.5 ± 0.7	47.1 ± 0.7	59.4 ± 8.0	51.1[d] ± 1.8
Co	1.16 ± 0.07	0.30 ± 0.05	0.26 ± 0.06	0.21 ± 0.01
Cs	5.58 ± 0.09	10.66 ± 0.15	8.32 ± 0.30	9.9[d] ± 0.8
Dy	4.29 ± 0.10	5.04 ± 0.12	4.23 ± 0.23	
Eu	0.64 ± 0.010	0.097 ± 0.006	0.129 ± 0.010	
Fe%	1.277 ± 0.014	0.733 ± 0.010	0.75 ± 0.03	0.72[d] ± 0.01
Hf	4.92 ± 0.07	4.43 ± 0.07	4.07 ± 0.10	4.11[d] ± 0.18
K%	3.58 ± 0.17	4.00 ± 0.22	3.86 ± 0.30	
La	29.7 ± 0.5	22.3 ± 0.5	29.1 ± 4.6	
Lu	0.362 ± 0.017	0.460 ± 0.020	0.360 ± 0.022	
Mn	276 ± 5	192 ± 4	175 ± 5	
Na%	3.30 ± 0.06	3.10 ± 0.06	2.90 ± 0.05	
Rb	145 ± 5	209 ± 7	186 ± 10	191[d] ± 7
Sb	0.17 ± 0.04	0.60 ± 0.06	0.56 ± 0.07	
Sc	3.39 ± 0.03	3.15 ± 0.03	2.78 ± 0.06	3.41 ± 0.14
Sm	4.58 ± 0.05	4.54 ± 0.05	4.51 ± 0.25	
Sr[e]	171 ± 26	<18 ±	<13 ±	
Ta	0.990 ± 0.010	1.671 ± 0.017	1.310 ± 0.064	1.51[d] ± 0.11
Th	10.54 ± 0.11	18.33 ± 0.18	16.02 ± 0.58	16.9[d] ± 0.9
U	3.21 ± 0.03	5.32 ± 0.04	4.37 ± 0.17	
Yb	2.54 ± .03	3.21 ± 0.04	2.64 ± 0.10	2.92[d] ± 0.28
Zr[e]	256 ± 38	125 ± 19	112 ± 17	[c]

[a]The measurements were calibrated with Standard Pottery whose composition and abundances are given in Ref. 6. The indicated errors are the precision (one standard deviation) of measurement. The accuracies can be deduced from the uncertainties in Standard Pottery given in the reference.

[b]The values in this column are the standard deviations measured in 7 Zinapecuaro obsidian rocks or the experimental error, whichever is larger.

[c]Ba and Zr data from Ref. 5 were not included because of uncertainties in these data.

[d]This value was normalized to the LBL calibration system with Teuchitlan and Etzatlan obsidian data.

[e]Measured by XRF.